POLITECNICO DI TORINO
Repository ISTITUZIONALE

On the effect of rapid annealing on the microstructure and mechanical behavior of additively manufactured stainless steel by Laser Powder Bed Fusion

(Article begins on next page)

20 March 2024

On the effect of rapid annealing on the microstructure and mechanical behavior of additively manufactured stainless steel by Laser Powder Bed Fusion

Mohammad Reza Jandaghi *,[1], **Abdollah Saboori** [2], **Luca Iuliano** [2], **Matteo Pavese** [1]

[1] *Department of Applied Science and Technology, Politecnico di Torino, Corso Duca Degli Abruzzi 24, 10129 Torino, Italy*

[2] *Department of Management and Production Engineering, Politecnico di Torino, Corso Duca Degli Abruzzi 24, 10129 Torino, Italy*

*Corresponding author; E-mail: **mohammadreza.jandaghi@polito.it**

Abstract

This work presents an investigation on the effect of rapid annealing on the microstructure evolution and mechanical performance of stainless steel 316L (SS316L) fabricated by Laser Powder Bed Fusion. In this process, it is well documented that the intensive thermal gradient in the heat flux direction leaves remarkable residual stress and promotes strong texture along the building direction (BD). In the current research, to swiftly reduce residual stresses, a short-term heat treatment at 1300 °C for different holding times of 10 to 120 s was designed and studied. Microstructural observation through the optical microscopy and scanning electron microscopy, as well as the X-ray diffraction analysis, revealed that rapid annealing longer than 30 s resulted in the gradual annihilation of the cell walls which are indeed the sub-grain boundaries (SGBs). In addition, electron backscatter diffraction outputs demonstrated that rapid annealing significantly reduced the low angle grain boundaries and attenuated the texture developed along the BD. Moreover, the analysis of grains size and shape illustrated that annealing up to 30 s recovered the structure. In contrast, longer annealing resulted in increasing the aspect ratio of grains along the direction with maximum residual strain (i.e. BD) due to activation of the strain induced grain boundary migration (SIGBM) mechanism. After the rapid annealing, the mechanical performance of the samples also indicated that annealing up to 30 s would not reduce the compressive and tensile strength more than 6%. In comparison, longer annealing resulted in 24% reduction in mechanical properties along with coarsening of dimples in the fracture surface of the samples.

Keywords: *Additive Manufacturing; Microstructure; Texture; Rapid Annealing; SIGBM.*

1. Introduction

Due to advantages such as excellent oxidation and corrosion resistance, notable mechanical strength, good formability and weldability, 316L stainless steel (SS316L) is widely used in biomedical and industrial applications **[1-4]**. Nonetheless, the low yield strength (YS) is usually the principal drawback of the SS316L components fabricated by conventional processes. Hitherto, different supplementary processes have been proposed to resolve this longstanding challenge **[5-7]**. However, the employed strategies often led to sacrificing the ductility in strength-ductility trade-off **[8]**. Hence, it is believed that a modern production method with more advanced capabilities to extend the mechanical strength of low-carbon austenitic steels should be exploited. For this reason, advanced manufacturing technologies such as Additive Manufacturing (AM) technologies are considered as promising alternatives to conventional manufacturing processes. In fact, through these technologies, it would be possible to not only improve the mechanical performance of the SS316L component but also to produce SS316L components with a high level of complexity **[9]**.

Laser Powder-Bed-Fusion (L-PBF) process uses Computer-Aided Design (CAD) data to build complex shape components via a layer-by-layer process **[10, 11]**. In this process, after spreading a thin layer of metal powder on the building platform or on the already solidified layers, irradiation of a high-intensity laser beam leads to a selective fusion of the particles according to the CAD data. In each layer, as the successive layers consolidate on previous layer, the building platform moves down equal to a layer thickness. This building process continues until the components reach the designed dimensions by CAD file **[12]**.

During L-PBF process, the extreme thermal gradients and high cooling rates can result in the generation of large residual stresses and consequently parts distortion **[13]**. According to the literature, in the rapidly solidified processes such as welding the level of residual stress is proportional to the thermal gradient and cooling rate. This problem becomes more serious in the L-PBF process, mainly owing to its nature as a rapid solidification process. Therefore, so far, several studies have been carried out to control residual stresses and minimize their value in L-PBF fabricated samples **[14]**. Nonetheless, often it is not possible to significantly reduce the level of residual stress through modification of the process parameters, particularly for laser printed SS316L samples **[15, 16]**. Hence, the post thermal treatment has been proposed as a low cost and reasonable supplementary process to relieve the residual stress and improve the performance of the L-PBF SS316L samples. Predominantly, post-printing

annealing of SS316L specimens is performed in a temperature range of 300-1200 ℃ for 30 minutes to 6 hours [17-19]. Reijonen et al [20] investigated the effect of applying different stress-relieving procedures and introduced the hot isostatic pressing as the most effective standardized heat-treatment for the 316L built components. Chao et al. [21] examined the annealing temperature of 400 ℃ and 650 ℃ for 2 hour and solution annealing at 1100 ∘C for 5 min. According to their report, applying such an annealing resulted in 24%, 65% and 90% stress reliving, respectively. Riabov et al. [22] declared that during annealing of the SS316L samples at 400, 800 and 1200 ℃, oxygen and nitrogen content gradually increases. In addition, by annealing the sample over 400 ℃, cellular structure was removed and elemental segregation at the cell walls was no longer detectable. It has also proven that, annealing up to 600 °C has not any major impact on the microstructure [23-25]. However, annealing between 600-1000 °C activates elemental diffusion and gradually eliminates the cell walls, leading to a sharp decline of mechanical strength. Keep on annealing above 1100 °C removes all L-PBF microstructure footprints and renders a conventional-like microstructure [23].

However, it is reported that long-term annealing is faced with two major challenges, such as grain growth and significant microstructural changes [26]. In fact, the high cooling rate during the L-PBF process results in a rapid solidification after the laser/material interaction and in the formation of an ultrafine sub-grain structure [27]. It should be highlighted that the presence of this ultrafine structure in the SS316L samples results in its superior properties. However, the long term annealing thoroughly removes such a desirable structure and thwarts the L-PBF supremacy [17]. Furthermore, AM techniques typically benefit from the exclusion of multiple time-consuming steps in the production cycle and combination with a long-term complementary procedure will reduce their productivity. Thus, in this study, the authors applied a rapid annealing heat treatment at elevated temperatures on L-PBF SS316L samples. Microstructural observations were characterized using Optical Microscopy (OM), Field Emission Scanning Electron Microscopy (FE-SEM) equipped with Electron Backscatter Diffraction (EBSD) detector and Energy Dispersive Spectroscopy (EDS). Phase evolution and lattice distortion were detected by X-ray Diffraction pattern (XRD) analysis. To find the correlation between the structural transformations and the mechanical behavior of the rapid annealed samples, tensile and compression tests were employed. In the current research, the authors surveyed the potential of rapid annealing as an effective way for relieving the residual strain in L-PBF fabricated SS316L samples along with preserving mechanical strength.

2. Experimental procedures,

2.1. Samples preparation

In this work, a spherical, gas atomized SS316L powder was used as a feedstock material (**Fig. 1(a)**).
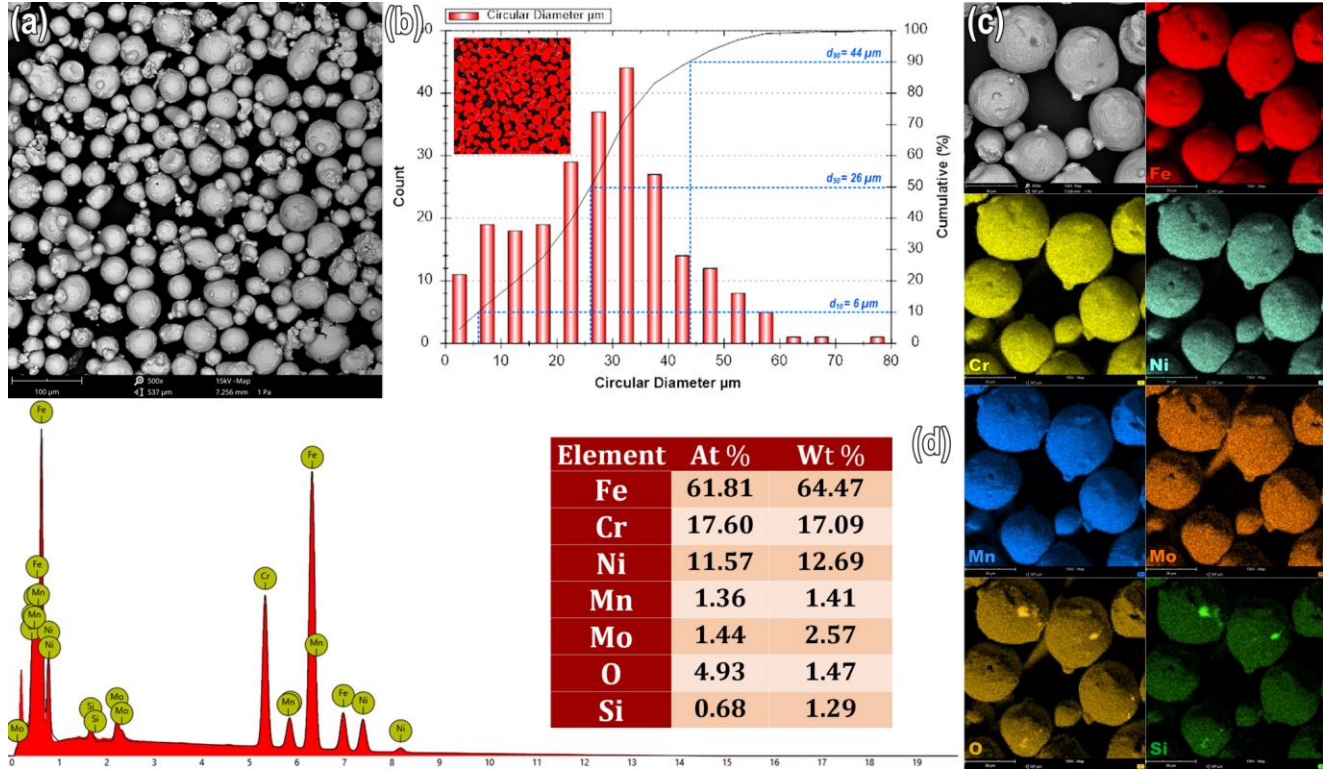

Fig. 1. SEM micrograph (a), size distribution diagram (b), element distribution map (c) and EDS elemental analysis (d) of the steel 316L powder used in L-PBF process.

The PSD of the starting powder was analyzed using PAX-it software, and the result is presented in **Fig. 1(b)**. As can be seen, the particle size range of the starting powder lies in the range of 15-65 μm, which is a typical particle size range for L-PBF. The chemical composition of the atomized powder is presented in **Fig. 1(c).** The samples were manufactured using a Sharebot METALONE Laser printing machine, equipped with a fiber laser with a wavelength of 1080 nm, maximum laser power of 250 W, the maximum scanning speed of 5 m/s and spot size of 40 μm.

Here, cubic samples with a dimension of 10×10×10 mm were fabricated using a stripe pattern and 90° rotation after printing each layer. Schematic illustration of the scanning strategy is depicted in **Fig. 2**.
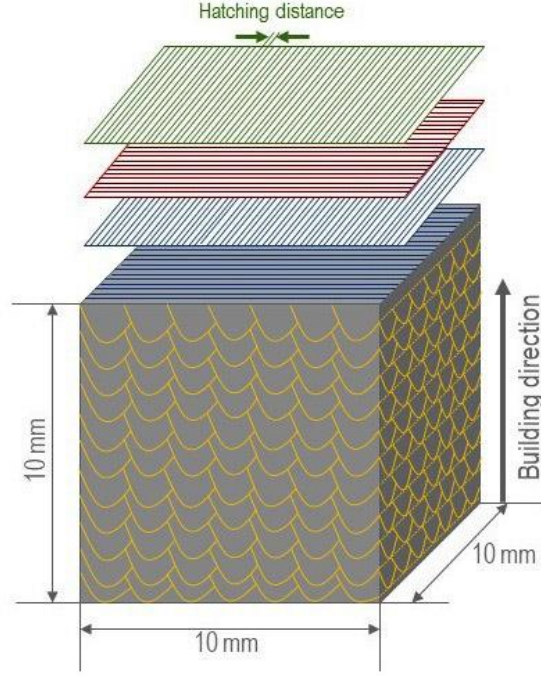
Fig. 2. Schematic representation of the samples fabricated with L-PBF method.

Before producing samples, a Design of Experiments (DoE) considering a different combination of process parameters was performed. As a result, the optimum process parameters to produce dense samples were achieved. In this DoE, several cubes were produced using a constant hatching distance of 100 μm, and a layer thickness equal to 30 μm. The laser power varied between 70 and 100 W, and the scan speed between 300 and 400 mm/s. To evaluate the effect of the combination of process parameters, the Volumetric Energy Density (VED) was considered and calculated using the following equation [28]:

$$E = \frac{P}{v \times d \times t}$$ (1)

where P is the laser power (W); v the scanning speed (mm/s); d the hatching distance (mm) and t the layer thickness (mm). In this work, to facilitate the sample removal and guarantee the mechanical support and heat dissipation, the samples were produced on support structures. After the building, all the cubes were removed from the building platform using Wire Electrical Discharge Machining (EDM). **Fig. 3(a-b)** shows the images of the as-built cubes for the microstructural analysis and compression test, and flat tensile samples, respectively.
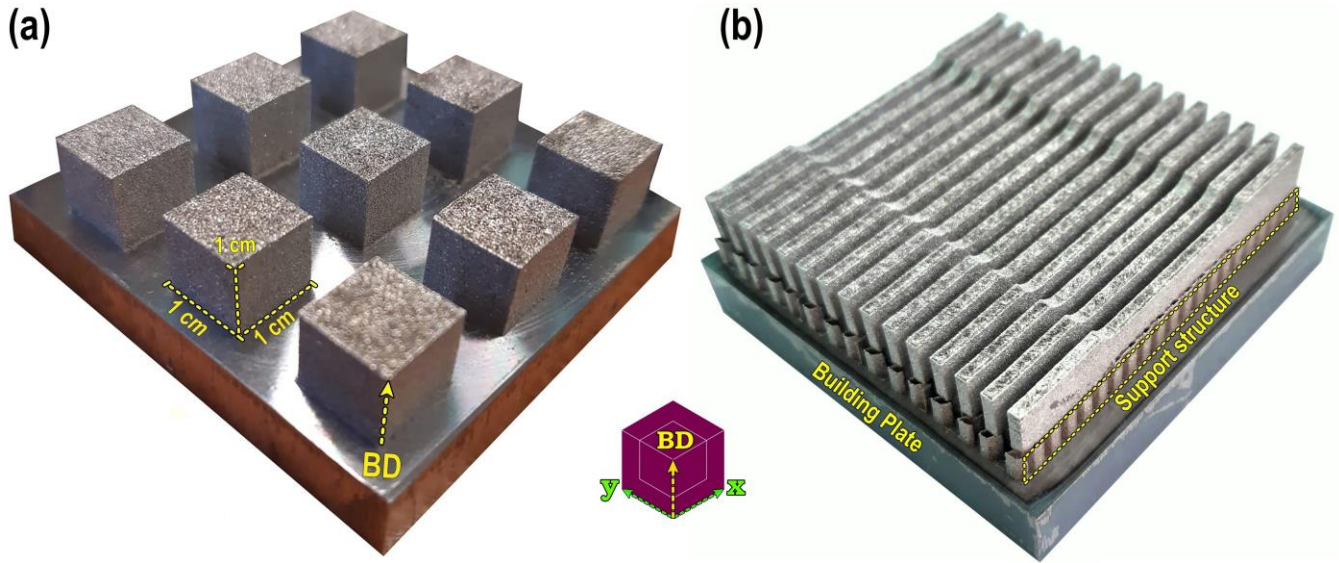
Fig. 3. Image of the 3D printed samples through L-PBF.

According to the literature, a temperature range of 800 to 1200 ℃ and an annealing time of 30 to 120 min have been usually considered for the solution treatment of L-PBF stainless steel specimens [27]. Instead, in this work, due to the higher kinetics of restoration at elevated temperatures, the samples were annealed at 1300 ℃ for 10 to 120 s followed by air cooling down to room temperature. In fact, the goal of this rapid heat treatment was to relieve the residual stress in a short time with a minimum change in the microstructure and mechanical properties of the as-built SS316L samples.

2.2. *Microstructural and mechanical performance evaluation*

The morphology and composition of the as-received powder and as-built SS316L samples were analyzed using a Carl-Zeiss FE-SEM equipped with an EDS analysis detector. For the microstructural analysis, both XY and XZ cross-sections of the as-built cubes were cut, ground and polished according to the standard procedure for the metallography of 316L stainless steel [29]. Thereafter, the porosity content of the samples was evaluated on the as-polished samples using Image Analysis method. To reveal the microstructure, all the samples were chemically etched in a solution composed of 50 vol.% hydrochloric acid, 40 vol.% nitric acid and 10 vol.% acetic acid for 10 s. A Leica DMI 5000M Optical Microscope (OM) was used to trace the microstructural variations. Structural transformations were evaluated using a PANalytical X'Pert PRO X-ray Diffractometer (XRD) equipped with a Cu-Kα radiation source (λ = 0.15406 nm) over a 2θ range from 35° to 100°. Effect of rapid annealing on the grain size

distribution and crystallographic orientation of the L-PBF fabricated specimens were probed by Electron Backscatter Diffraction (EBSD) analysis. The EBSD measurements were carried out using a JEOL 7000 FE SEM system equipped with a detector for EBSD. The EBSD measurements were performed at an acceleration voltage of 20 kV and a step size of 1 μm. The AZTEC data acquisition software (Oxford Instruments plc) was employed in this work. The outputs were analyzed by TSL Orientation Imaging Microscopy (OIM) Analysis 7 software from EDAX. EBSD mappings of the as-built and subsequently annealed samples were sectioned along the Building Direction (BD)-Transverse Direction (TD) plane. Mechanical properties of the samples were evaluated via tensile and compression tests employing an Instron 8562 device with a crosshead velocity of 2 mm/min. For each sample, at least three specimens were examined to ensure the repeatability of the results. In order to explore the effect of the annealing on the mechanical performance of the SS316L samples, tensile and compressive Yield Strength (YS) and Ultimate Tensile Strength (UTS) of the heat-treated specimens were measured and compared with those of as-built ones.

Results and Discussion

2.3. Process parameters optimization

Fig. 4 displays the OM cross-section of the as-polished SS316L cubes produced using various combination of process parameters.
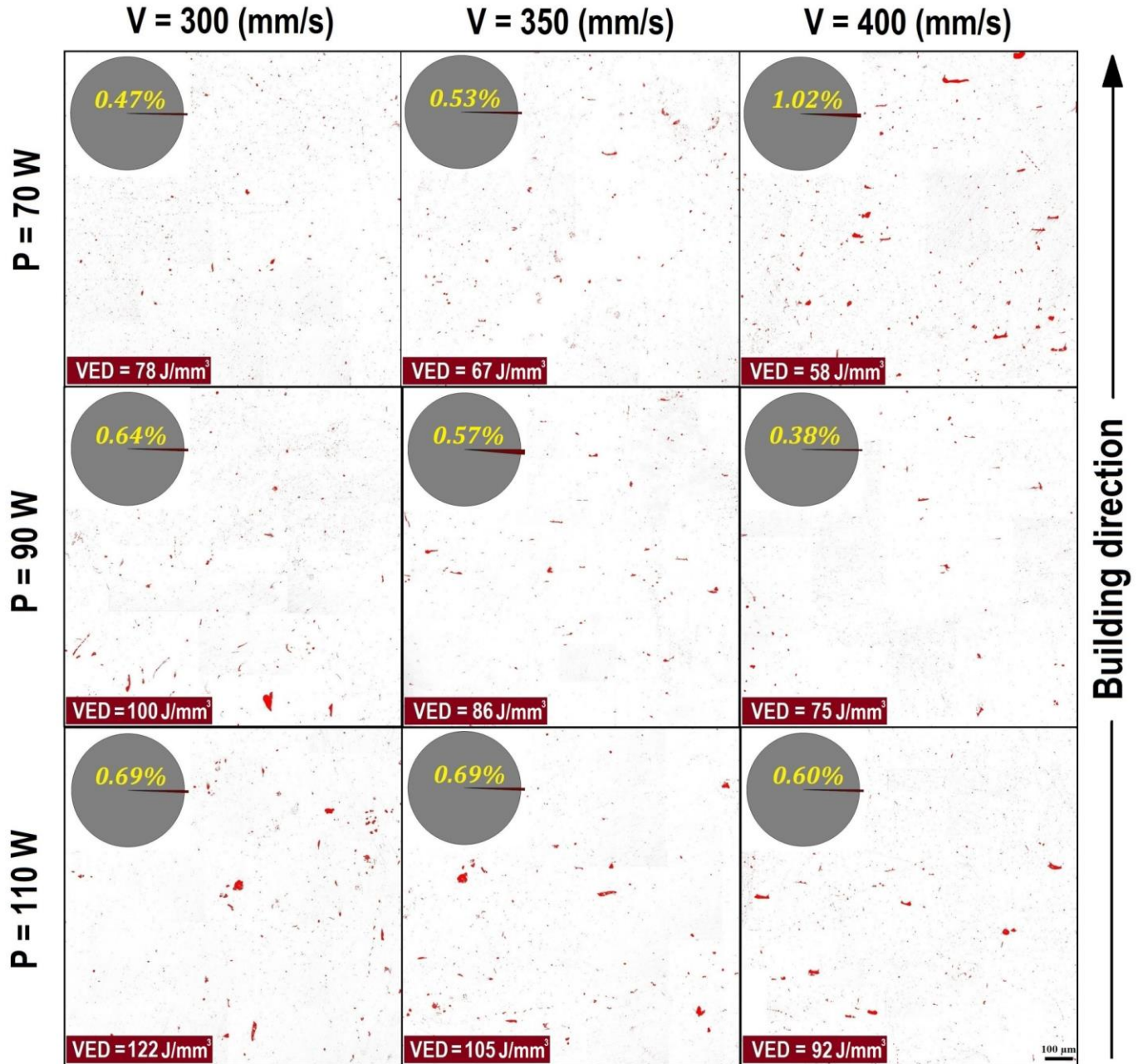
Fig. 4. Effect of different scanning speed (*v*), laser power (*w*) and energy density (VED) on the variation of porosity fraction along building direction in BD-TD plane.

As shown in this figure, the samples porosity content calculated through image analysis lies in the range of 0.47-1.02%. Moreover, **Fig. 5** exhibits volumetric porosity variation as a function of energy density. It is evident that in the samples produced with the lowest laser power (70 W), the porosity content increases by increasing the laser scanning speed. The presence of irregular shape porosities in these samples suggests that the energy density provided to the material for melting was insufficient and as a consequence resulted in the formation of process-induced porosity that is also known as lack of fusion porosity (LOF) **[30]**. It is evident

that by increasing the energy density up to a certain level, it would be possible to facilitate the SS316L samples consolidation, leading to a very low porosity content in these samples.
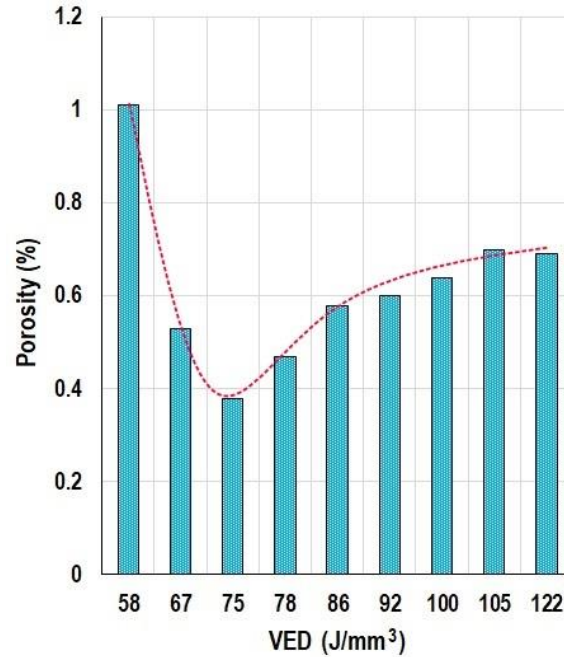

Fig. 5. Variation of porosity fraction as a function of energy density (VED) for samples fabricated by different processing parameters.

On the other hand, it was found that raising the energy density to more than ≈ 80 J/mm³ was accompanied by the formation of gas induced-pores in the as-built SS316L cubes. Formation of this type of porosity in the as-built samples can be due to evaporation and entrapment of some alloying elements [31]. **Fig. 5** indicates that the densest sample, with minimum porosity content, could be achieved utilizing an energy density between 70 to 80 J/mm³. This optimized range for energy density would be reliable until the other processing parameters remain constant. It means that by any change in the layer thickness, scanning strategy, laser beam diameter and morphology of feedstock material from the optimized condition, a slight re-optimizing might be required [32].

Microstructural evolutions during rapid annealing

Fig. 6 shows the general microstructure of the SS316L cube produced using the optimum process parameters. Accordingly, the grains nucleated on the support structures were finer than those in the middle of the cube. Formation of these fine grains at the bottom of the samples is due to the presence of a cold building platform that acted as a heat sink. Due to the

higher cooling rate at the primary layers, the formation of finer grains near the building plate was expectable. After printing the initial layers, gradually the role of the building platform in dissipating the laser heat became less effective, resulting in heat accumulation in the center of the samples. This accumulated heat promotes epitaxial grain growth in the direction of the maximum thermal gradient. Formation of this type of microstructure in the as-built SS316L samples is also consistent with the results reported by Andreau et al. **[33]**. In fact, they proved that in the first layers, the grains were finer with random orientation while after some initial layers, the grains continue to grow along a preferential direction, creating a strong texture along the BD (**Fig. 6(b)**).
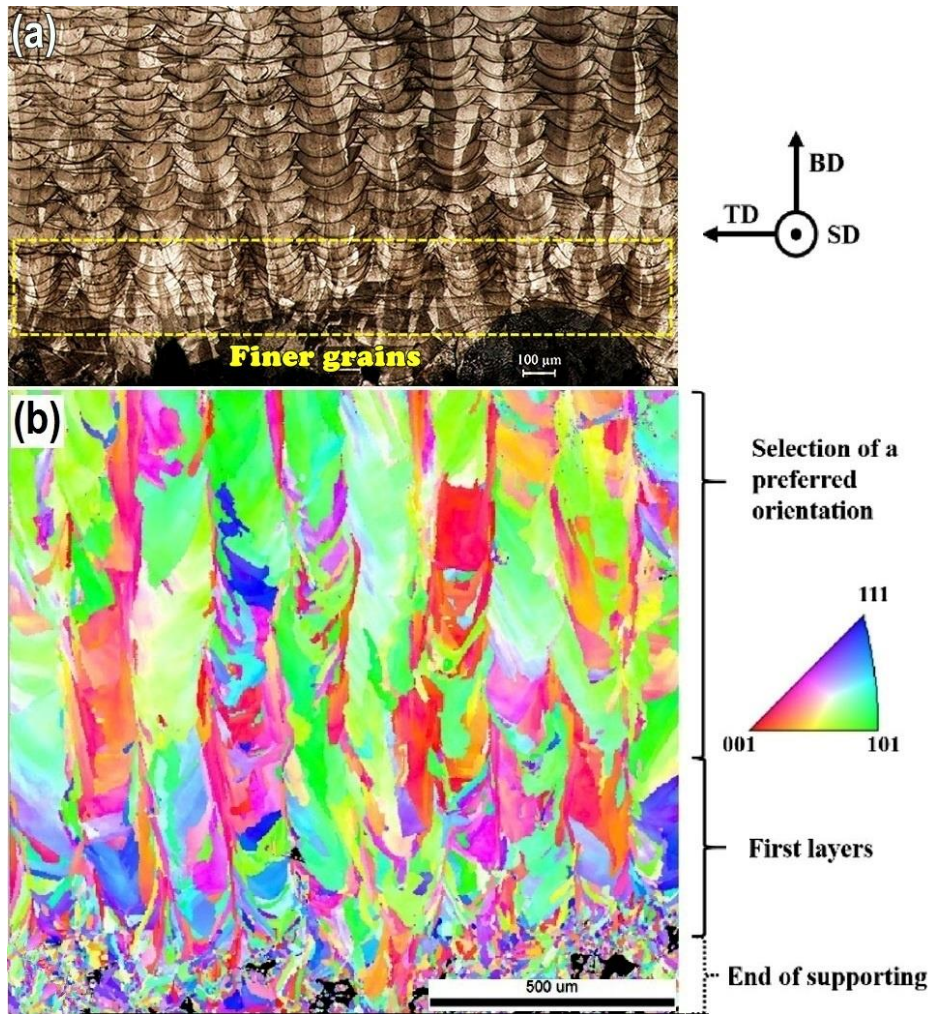
Fig. 6. (a) Optical micrograph, and (b) EBSD colour map [33] representing the grains morphology and orientation from bottom to center of the as-built SS316L specimen.

Fig. 7 compares the 3D OM micrographs of the L-PBF SS316L samples before and after the rapid annealing at 1300 °C for different periods of time, from 10 s to 120 s. The top surface of the specimens (*XY* plane) indicates that laser tracks are intersecting at an angle of 90°, which

is equal to the rotation angle per layer during the building process. Besides, fine equiaxed grains observed in the *XY* plane are indeed a transverse section of the columnar grains that have grown along the BD. As already discussed, it is well documented that the formation of the elongated grains along the BD is usually due to the presence of a high thermal gradient along the BD that results in a directional heat dissipation [34]. It is evident that by increasing the annealing time the columnar grains grew, and the melt pool boundaries faded gradually until they completely disappeared after 120 s.
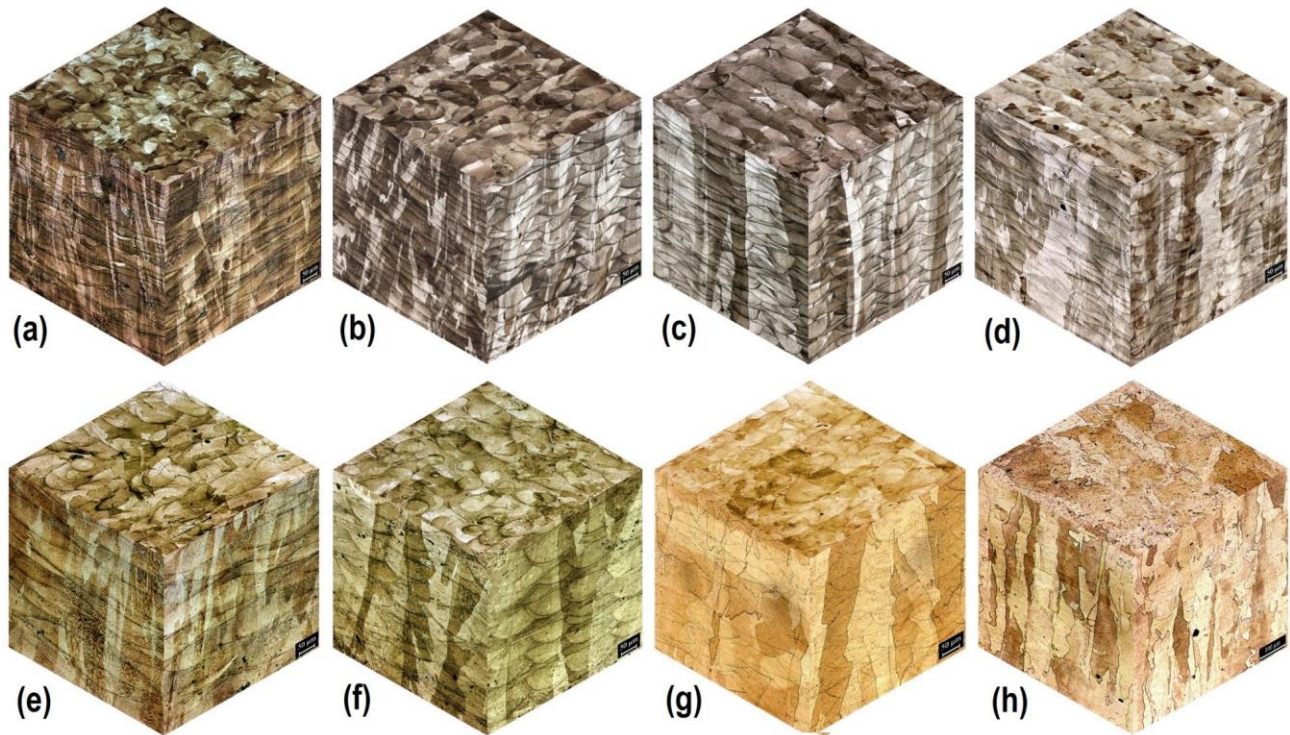

Fig. 7. OM micrographs of the L-PBF SS316L sample, (a) in the as-built state, after heat treatment at 1300 °C for (b) 10 s, (c) 20 s, (d) 30 s, (e) 45 s, (f) 60 s, (g) 90 s and (h) 120 s.

FE-SEM micrographs in **Fig. 8** represent the effect of heat treatment on the cellular and dendritic structures formed inside the melt pools during the L-PBF process. In fact, as reported in the literature, the final microstructure of an AM sample can be defined by the local solidification rate, the temperature gradient at the solid-liquid interface (G), the growth rate of the solidifying front (R), the undercooling ($\triangle T$) and the alloy composition. In particular, the solidification mode and consequently the morphology of the final microstructure depends on the solidification morphology parameter (G/R) and the cooling rate level ($G \times R$) [35].

Notwithstanding some local variations in the microstructure of the as-built sample, the high cooling rate in the L-PBF process, that can reach 10^5-10^6 K/s, contributes markedly to the microstructure refinement and, as a consequence, to the higher mechanical properties compared to the conventionally manufactured alloy [36]. It is also proved that this kind of cellular-columnar structure can be formed only when G/R is higher than $\Delta T/D$, where ΔT is the solidification undercooling and D is the diffusion coefficient of the printed material. Notwithstanding this knowledge, still the prediction of the microstructural features of SS316L L-PBF samples based on the process parameters is a vital challenge. In particular, the local changes in G and R values during the building process can lead to the formation of columnar or equiaxed microstructures in the as-built samples. **Fig. 8(a)** illustrates a representative microstructure of the SS316L samples, including cellular and elongated dendrites and the melt pool boundaries in the as-built microstructure of the SS316L samples. Interestingly, as shown in **Fig. 8(b)**, both the cellular structure and the melt pools boundaries were stable after annealing up to 30 s. Instead, a substantial microstructural transition started after 45 s by the partial coalescence of the melt pool borders (**Fig. 8 (c-d)**). **Fig. 8(e-f)** indicate that at longer annealing, up to 90 s, the melt pool contours disappeared, resulting in the homogenization of the microstructure.
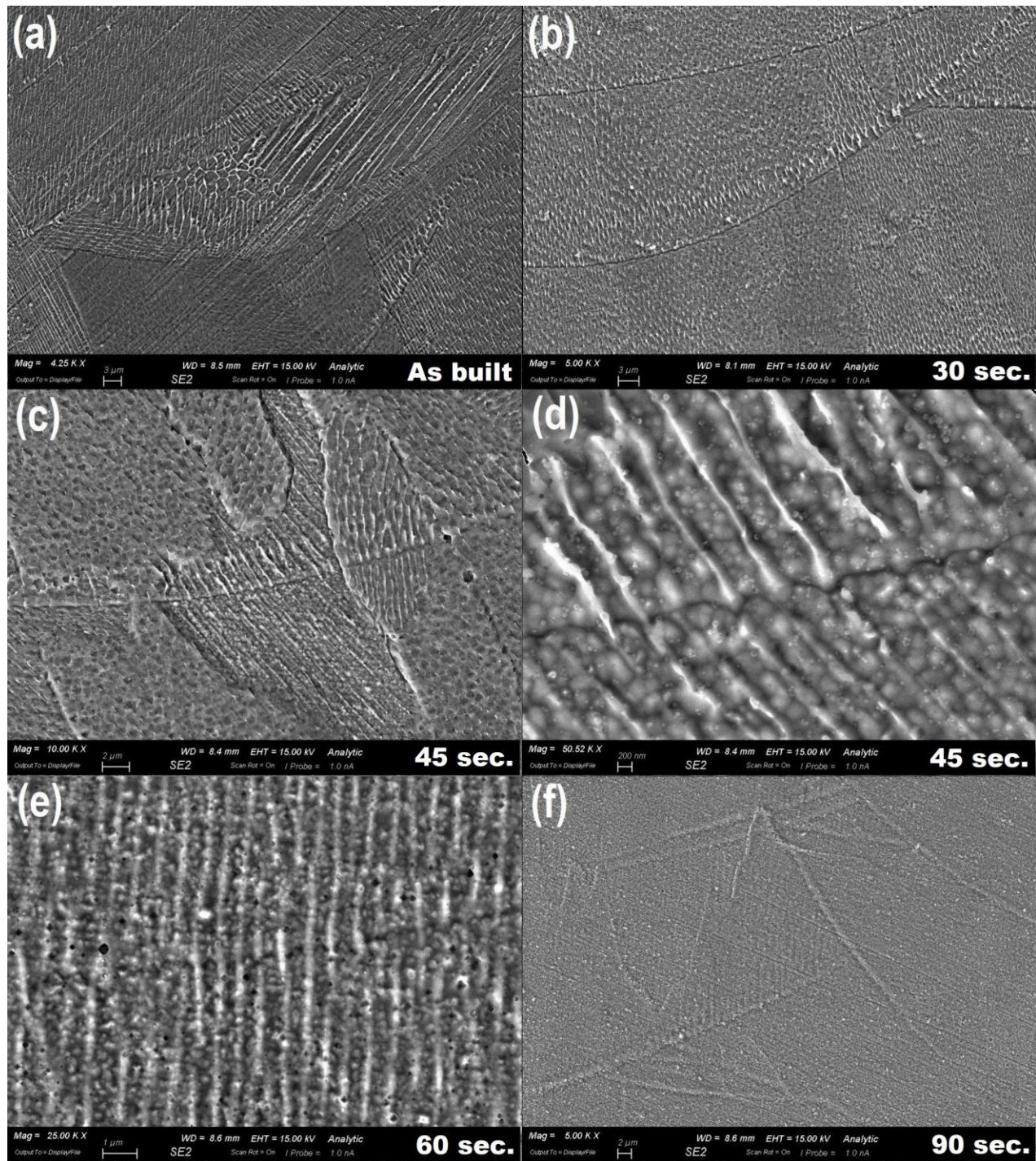
Fig. 8. Melt pools evolution in L-PBF SS316L samples, (a) in the as-built state, after annealing at 1300 ºC for (b) 30 s, (c-d) 45 s, (e) 60 s, and (f) 90 s.

Fig. 9 shows the SEM image of the as-built SS316L samples indicating the formation of a zigzag pattern during the epitaxial grain growth by passing through the successive layers. To minimize the nucleation energy during the solidification, the grains of the new layer preferentially continue the growth path of the previous grains. Moreover, during the building

process, because of using 90° rotation per layer, in each new layer the laser trajectory is perpendicular to the previous layer. As a result, the growth orientation of the grains as well as their internal columnar dendrites rotates toward the maximum thermal gradient, which is generated by the heat source. Consequently, cellular structure as elongated tubes with polygonal cross-section were formed along the thermal gradient direction (**Fig. 9(b)**). Where the laser tracks of the subsequent layers overlap, the grains and dendritic structure resumes the growth pattern of the previous layer (**Fig. 8(d-e)**).
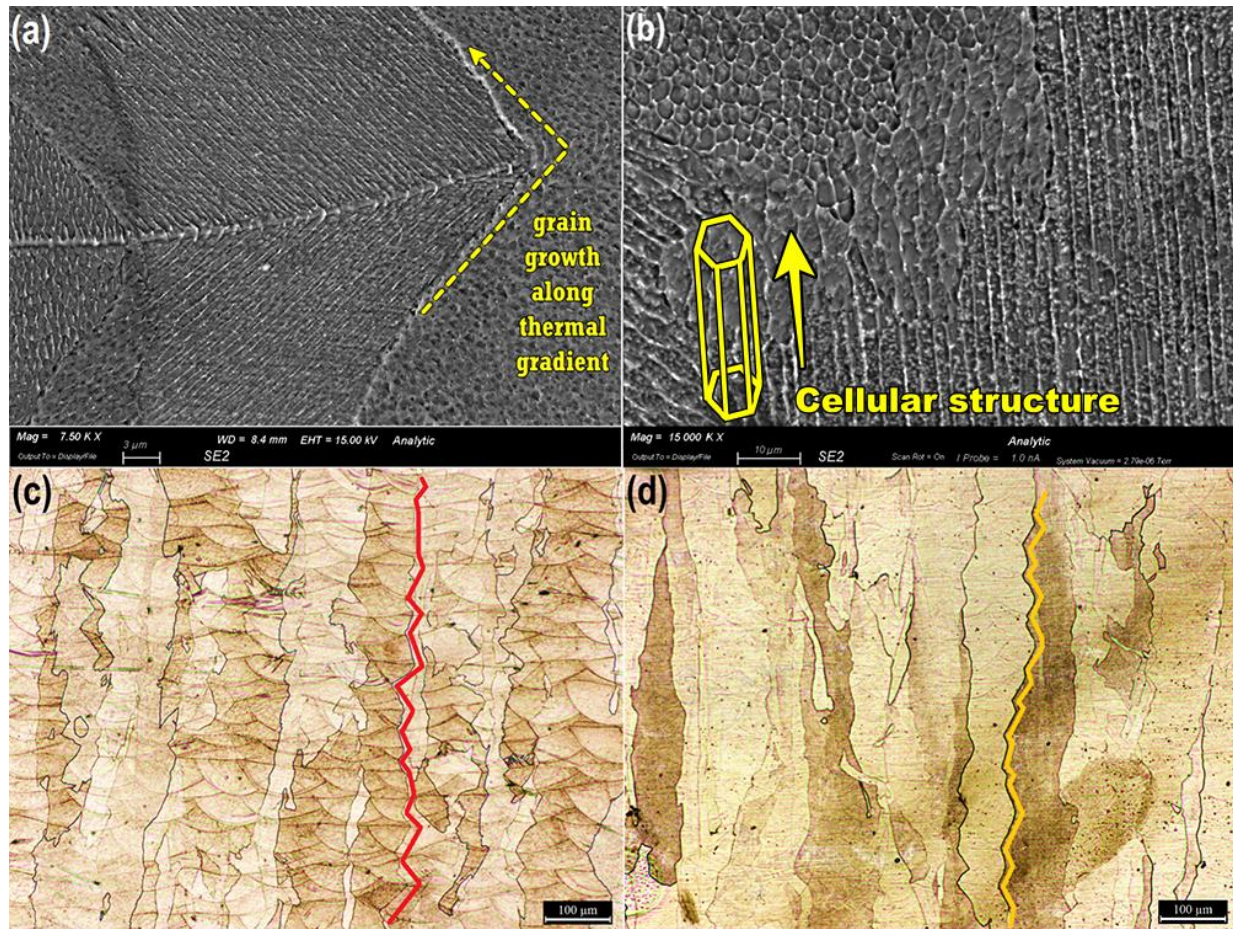
Fig. 9. (a) Zigzag epitaxially grain growth during L-PBF, (b) Schematic of cellular growth during L-PBF, and (c) stability of the fish scale pattern after annealing for (c) 90 s and (d) 120 s.

In general, thus, the fish-scale pattern originates from a successive change in the growth direction of the grains by passing sequential melt pools during the epitaxial growth. It is interesting to point out that this pattern remained stable during the rapid annealing, even

after the heat treatments over 45 s that gradually unified the melt pools and eliminated the laser runways (**Fig. 9(c-d)**).

Fig. 10(a) is a representative SEM micrograph of the as-built SS316L sample produced via L-PBF process. As can be seen, the cell size of the as-built sample that was measured using triangle method **[37]** is 0.75±0.09 μm. Kim et al. **[38]** and Yin et al. **[39]** found that the cooling rate during the solidification is the key parameter that defines the cell size, and their correlation can be expressed as follow:

$$\lambda_1 = A \, \beta^{-D} \qquad\qquad (2)$$

Where λ_1 is the cell size, in μm, and β is the cooling rate, in K/s. A and D are two parameters, with values in the range A = 10^2-10^4, and D = 0.25-0.7. In the literature, this equation is well adapted to assess the relationship between the cell size and cooling rate for various stainless steels, with $A = 80$ and $D = 0.33$ **[40]**. Therefore, here the cooling rate during the solidification was also estimated using this equation and the cell size calculated via image analysis. The outcomes of this evaluation indicated that the formation of 0.752 μm cells resulted from a cooling rate equal to 1.2×10^6 K/s. It is very interesting to notice that the calculated cooling rate in this work is in a good agreement with those of literature **[41]**.

The influence of rapid annealing on the cellular structure is presented in **Fig. 10(b-d)**. The comparison of **Fig. 10(a-b)** illustrates that the cellular network's size and morphology remained stable during the rapid annealing up to 30 s. As the annealing time extended, the cell walls gradually disintegrated, and after 60 s, they disappeared to a large extent (**Fig. 10(c-d)**). Because of the high kinetic of lattice transformation at elevated temperatures, rapid annealing even for longer times did not change the initial size of the cellular structures until complete elimination of the cell walls **[42]**. According to Zhong et al., these cell walls characterized by a high dislocation density are the SGBs **[43]**. In fact, the aggregated dislocations in the SGBs are essentially immobile and can only move by glide mechanism **[23, 44]**. Hence, they displayed higher stability during heat treatment and were eliminated at high temperatures only for longer periods.
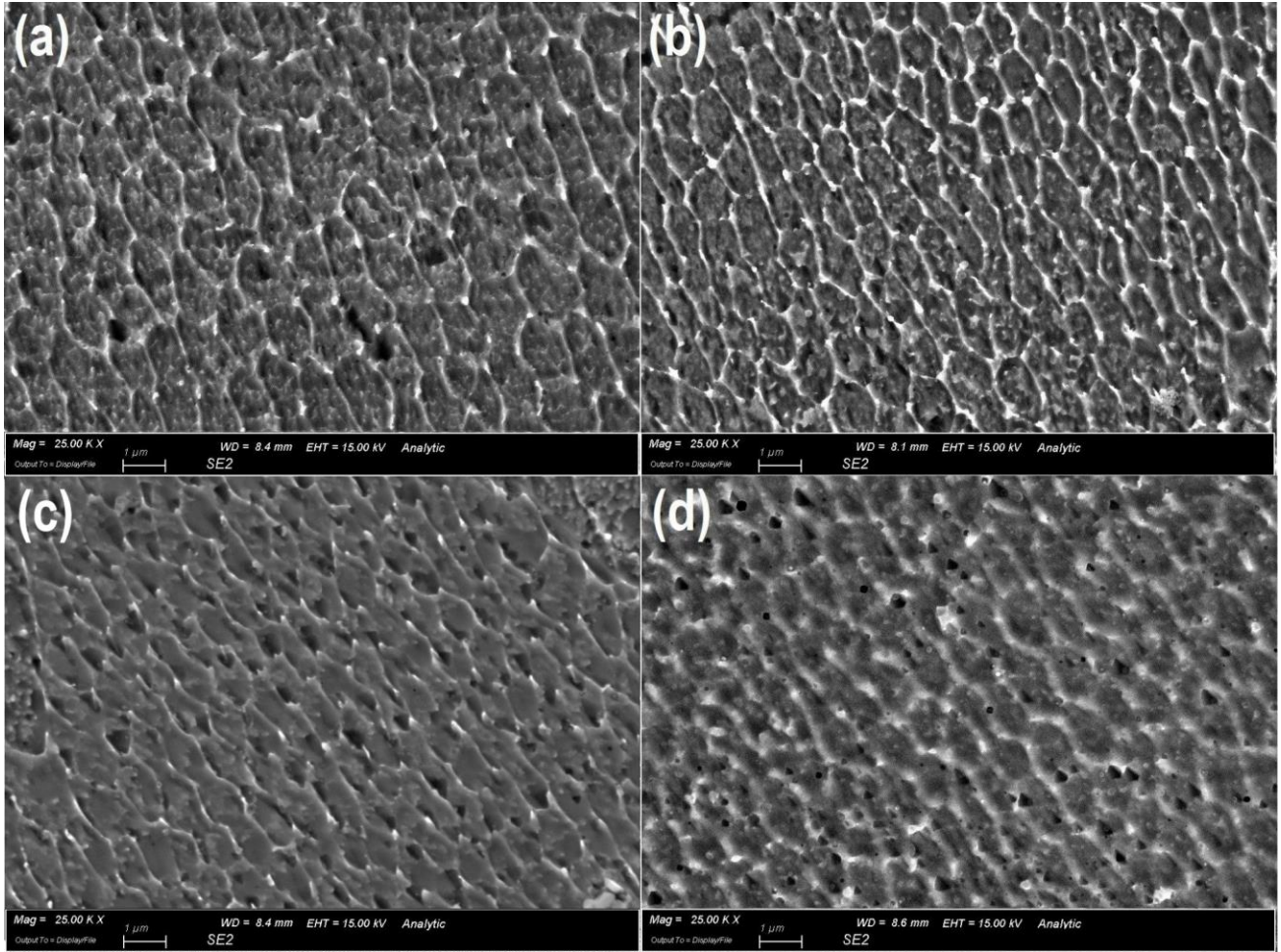
Fig. 10. SEM micrograph of the cellular structures in (a) as-built state, after annealing at 1300 ºC for (b) 30 s, (c) 45 s, and (d) 60 s.

Apart from the cell size, it is also believed that the cooling rate has a vital effect on other microstructural features of the as-built samples. In general, standard rapid solidification of an austenitic stainless steel can lead to the formation of two microstructures, according to its chemical composition; austenite (γ) and δ-ferrite **[45]**. In fact, during the L-PBF process, since the cooling rate is much higher than in the case of conventional manufacturing processes, the molten material solidifies in a non-equilibrium state. As a result, the prediction of the phase composition of the as-built samples are very challenging. In the literature, Schaeffler diagram and pseudo-binary predictive phase diagram have been used to roughly evaluate the phase composition and solidification mode of the SS316L during the rapid solidification **[46]**. In this work, in order to predict the theoretical gross quantity of δ-ferrite at first Cr and Ni equivalents were calculated using the equations that are presented elsewhere **[47]**. According to the Schaeffler diagram, pseudo-binary diagrams and equivalent contents of Cr and Ni, it was

16

found that the theoretical residual δ-ferrite content of the as-built samples should lie in the 5-10% range. Moreover, the ratio of $Cr_{eq.}/Ni_{eq.}$ was calculated to be 1.52. According to the pseudo-binary phase diagram and the calculated $Cr_{eq.}/Ni_{eq.}$ of the as-built samples, the SS316L alloy used in this work was placed within the FA region, i.e. that of austenite + lathy ferrite. It means during the solidification, the primary δ-ferrite solidifies in the melt pool. Thereafter, in the L+δ zone, the last fraction of liquid becomes rich in γ-stabilizer elements such as Ni, N and C, and solidifies later in the γ structure. However, it should be underlined that the presence of a rapid directional solidification together with the reheating of the solidified layers during the building process can promote the segregation of alloying elements and consequently the variation of the microstructural features. SEM images of **Fig. 11** confirms the presence of some white phases settled at the SGBs. In particular, EDS elemental analysis revealed that cell boundaries were decorated with Cr and Mo as well as a small amount of Si (**Fig. 11(c)**). There are various theories about the presence of Si in the SGBs. Salman et al. **[18]** suggested that since Si is a ferrite stabilizer, it probably leaves the liquid phase during the solidification and precipitates at the SGBs. Saeidi et al. proved that during solidification, Si and Cr migrate from the adjacent areas to cell walls and form spherical amorphous nano-inclusions **[36]**. The simultaneous presence of Ni, Mo and Cr-containing silicate nano-inclusions can play a synergistic pinning role at the SGBs. As a result, intertwined stabilized dislocations in cell boundaries will act as a strong barrier to the movement of free dislocations. Recent studies have also confirmed that cellular network can enhance the resistance of materials to deformation by delaying or preventing the migration of free dislocations formed under external force **[17, 48, 49]**.
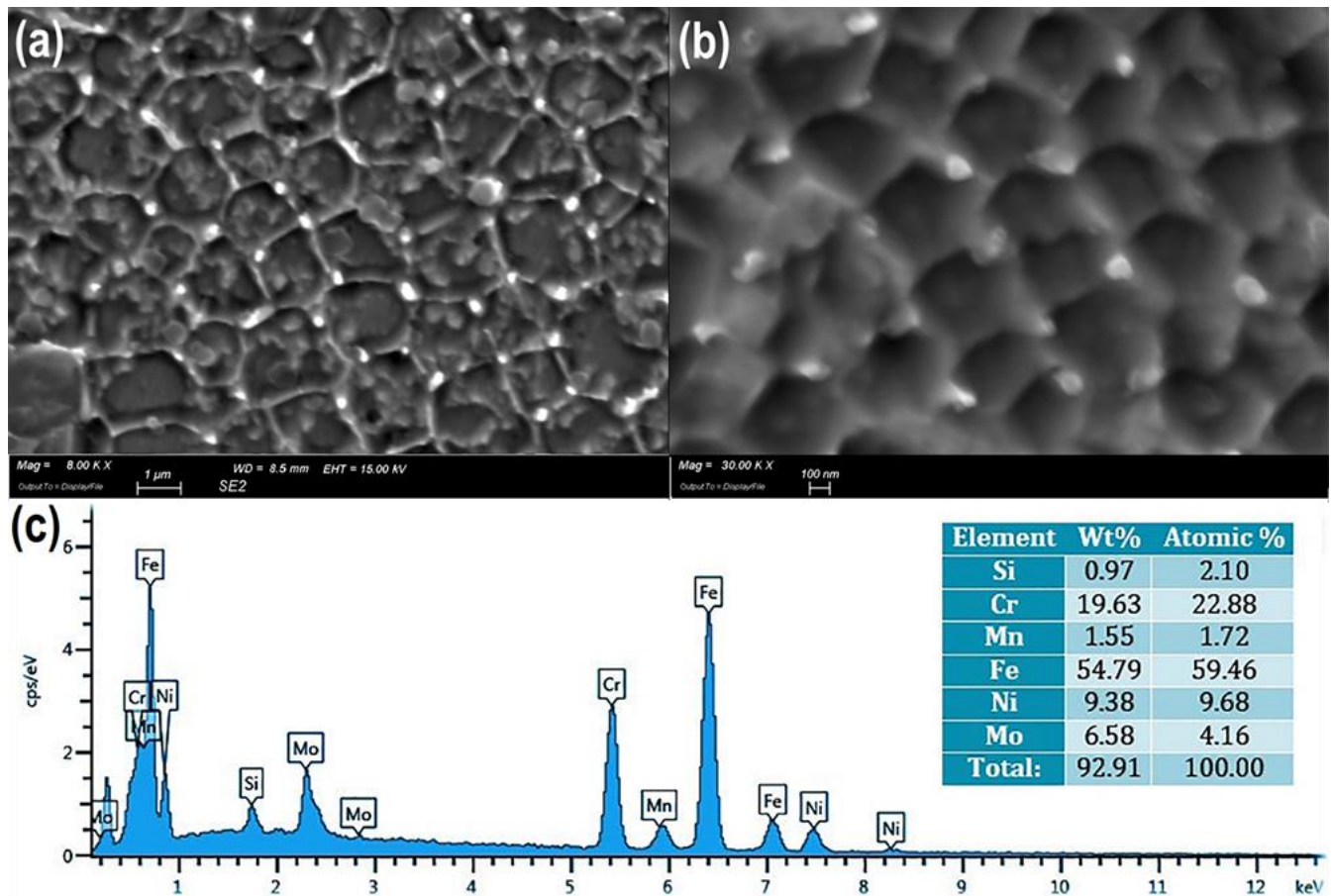
Fig. 11. (a) Accumulation of heavy elements on the cell boundaries (in white colour) and (b) at higher magnification; (c) EDS elemental analysis of the white phase depicted in (b).

The comparison of the XRD patterns of the atomized powder with the as-built specimen through L-PBF suggests that the quantity of the primary δ-ferrite in the as-built SS316L sample was slightly lower than in the SS316L powder (**Fig. 12(a)**). On the other hand, structural analysis via SEM equipped with EBSD detector verified the presence of a slight amount of δ-ferrite on the cell boundaries (**Fig. 12(b)**). Accordingly, the unevenly distributed green dots in the austenitic substrate (blue background) represent δ-ferrite with body-centred cubic (BCC) arrangement. As shown in **Fig. 12(c),** a high temperature annealing longer than 120 s could annihilate the cellular structure and facilitate the diffusion of stacked elements from the sub-grain boundaries into the austenitic substrate.
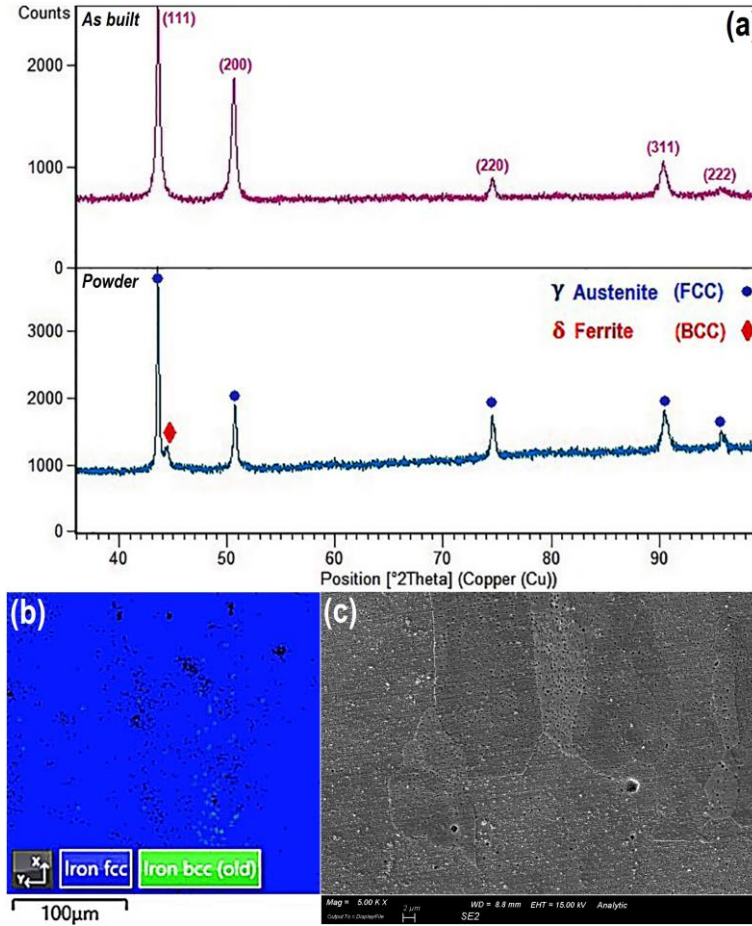
Fig. 12. (a) XRD pattern of initial powder and as-built sample, (b) EBSD output implying on random distribution of remained δ-ferrite by BCC structure in austenite matrix, and (c) complete annihilation of the cellular network after annealing at 1300 ºC for 120 s.
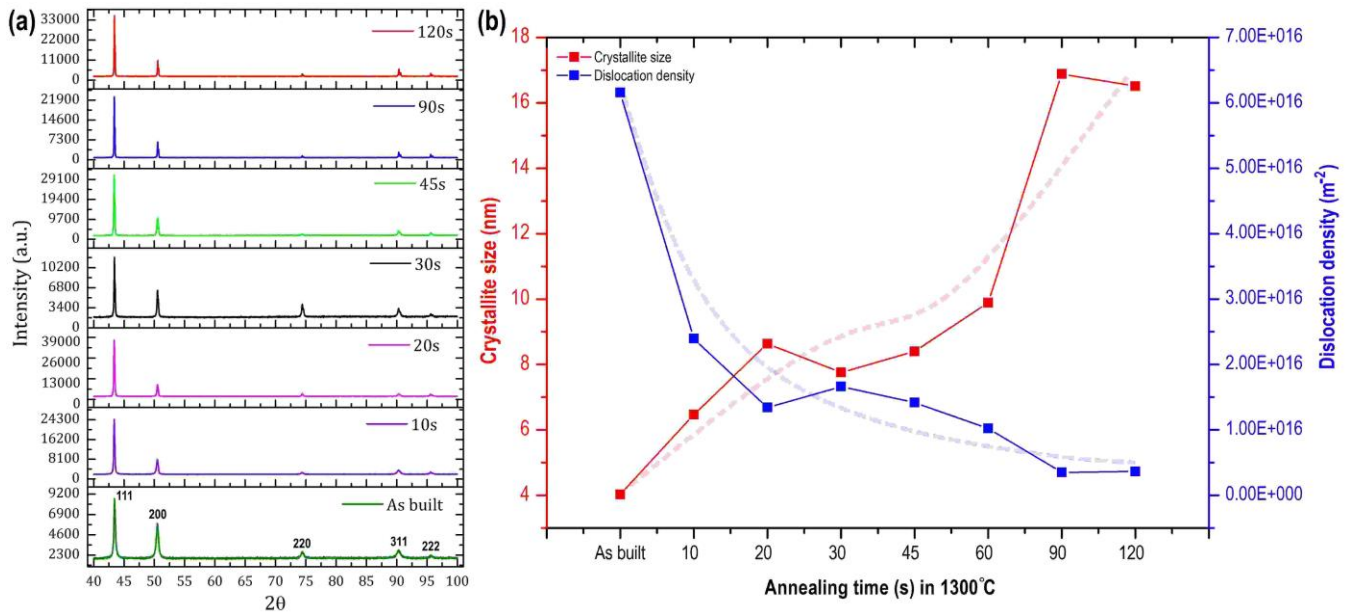

Fig. 13. (a) XRD patterns of the L-PBF fabricated samples after different annealing times and (b) changes of crystallite size and dislocation density during rapid annealing for different times.

XRD analysis that was performed on the samples before and after the heat treatment elucidates the lattice transformations during the rapid annealing **(Fig. 13)**. According to **Fig. 13(a)**, owing to the Faced-Centered Cubic (FCC) structure of austenite, regardless of specimen, (111) plane has the maximum peak intensity ratio (I/I_{max}) between atomic planes. Annealing up to 20 s is accompanied by the strong intensification of the (111) plane reflection. But, annealing at 30 s reduces the intensity of (111) plane again, with longer annealing times following the previous intensification uptrend. The calculation of the variation of crystallite size and dislocation density from the XRD spectra was executed by using Williamson-Hall and Scherrer methods, and the results are presented in **Fig. 13(b)**. It is very interesting to highlight that before and after the 30 s annealing, two different trends were revealed. In fact, annealing below 30 s evidently reduced the dislocation density and caused the growth of the crystallite, whereas, annealing for 30 s resulted in a transitory reversion of this trend. This discrepancy can be attributed to the thermal recovery and rearrangement of the free dislocations. As a matter of fact, as the annealing time increased, the twisty dislocations walls were gradually dissipated. This structural evolution emerged as a decrease in dislocation density along with an increase in crystallite size.
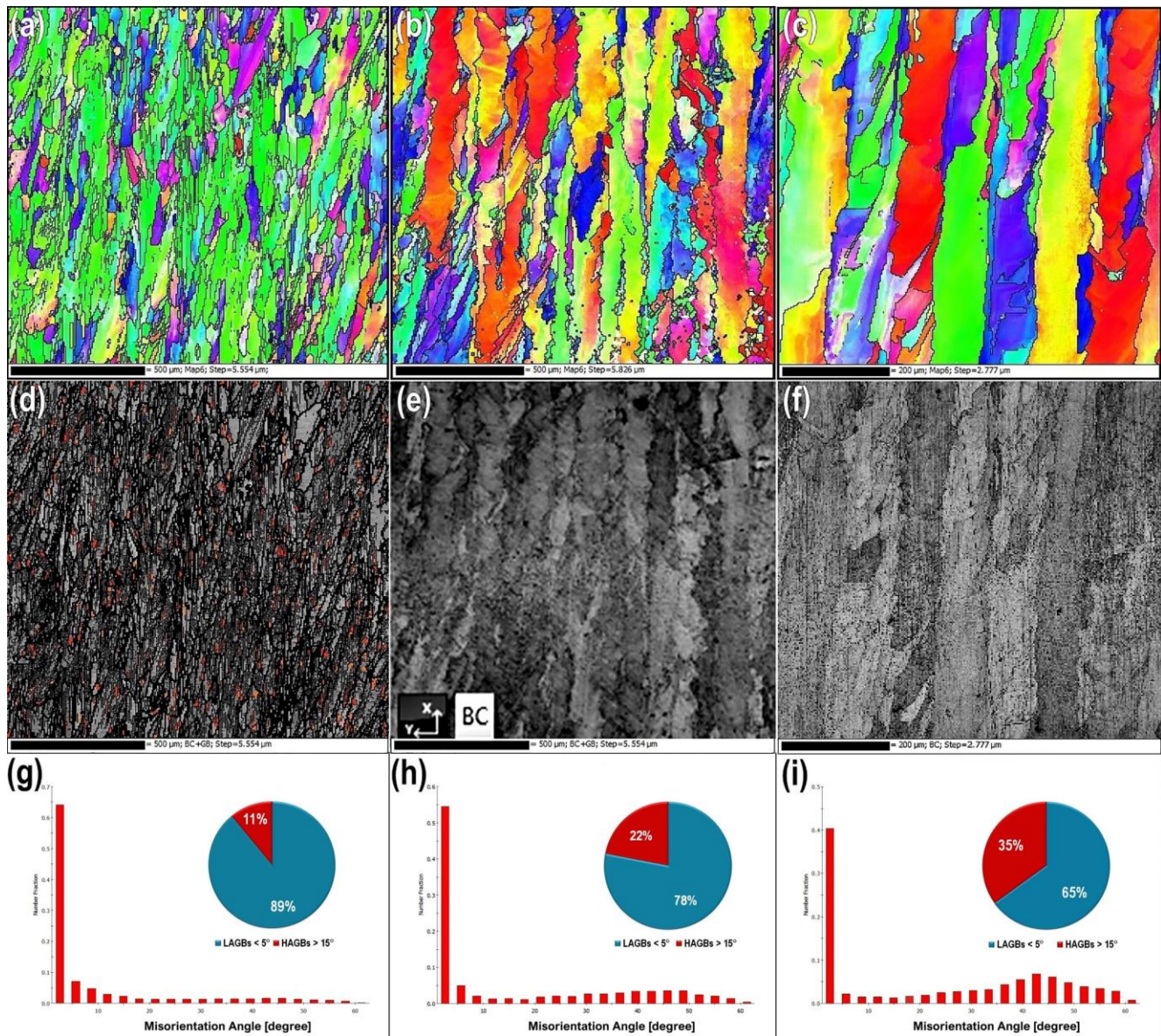
Fig. 14. (a-c) EBSD grain color map, (d-f) band contrast, and (g-i) misorientation profile of L-PBF fabricated SS316L samples after annealing for 45 s and 90 s at 1300 °C.

EBSD grain color maps of as-built SS316L specimen after 45 s and 90 s annealing at 1300 ℃ is displayed in **Fig. 14(a-c)**. Variation of color contrast in discrete grains can be attributed to the intergranular misorientation. Hence, the increment colors variety in the color map of EBSD images implies augmentation of the preferential orientations in many number of the grains and depression of the developed texture along the BD. Both small swerved and narrow columnar grains of opposite colors are probably formed in the overlap zone between the adjacent laser tracks. As can be seen in this figure, increasing the annealing time causes an increase of the grain size. The band contrast images of **Fig. 14(d-f)** reveals that annealing for

21

45 s has remarkably removed the SGBs and more annealing time could not make impressive changes in the structure. The variation of the misorientation profile for similar distances of specimens after different annealing times is presented in **Fig. 14(g-i)**. As can be seen, annealing for 45 s significantly increased the fraction of high angle grain boundaries (HAGBs), which means a huge number of low angles grain boundaries (LAGBs) are annihilated. However, doubling the annealing time did not tangibly increase the HAGBs. Comparison of this trend with SEM images of **Figs. 10** and **12** and dislocations trend in **Fig. 13** revealed that a continuous reduction in the dislocation density, the annihilation of cellular structure, and downtrend of LAGBs during annealing over the 30s occurred in accordance together.
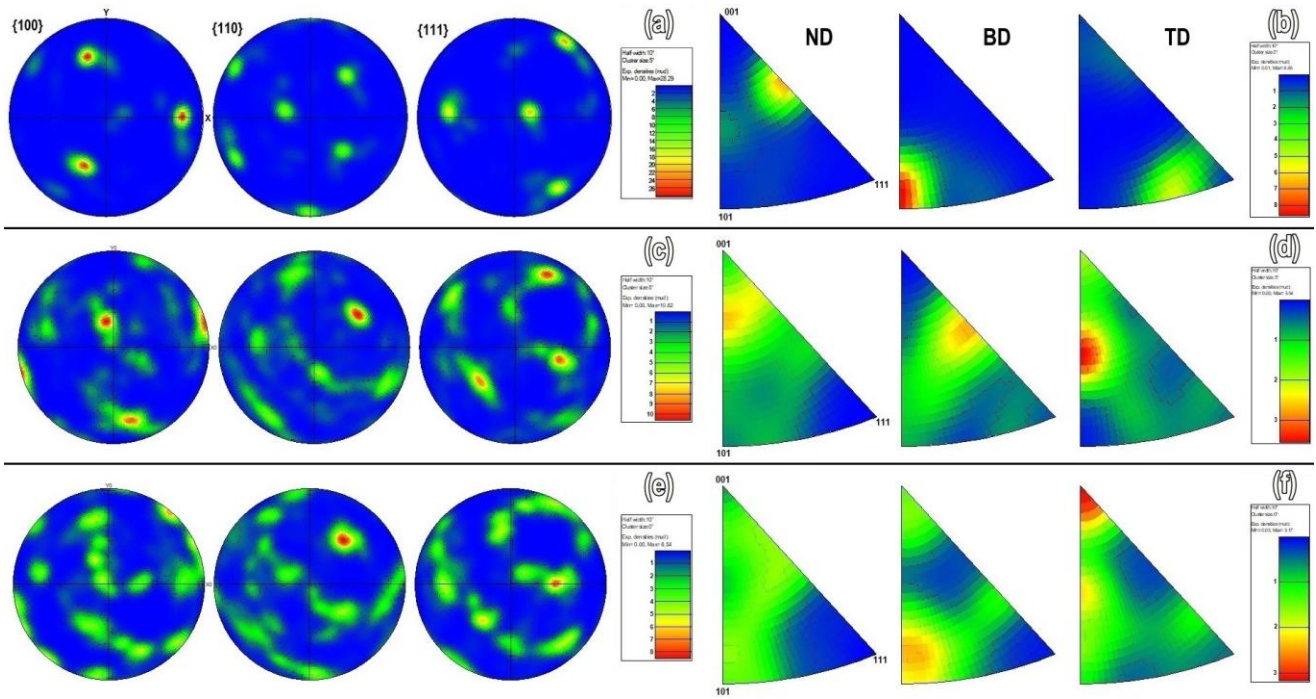
Fig. 15. (a,b) EBSD PF and IPF of the as-built SS316L, and after annealing for (c,d) 45 s and (e,f) 90 s.

In order to survey the effect of rapid annealing on the crystallographic texture and preferential orientation of the grains, the stereographic texture pole figures (PF) and their corresponding inverse pole figures (IPF) were investigated in the samples before and after the heat treatment (**Fig. 15**). The center of pole figures is parallel to the building direction (normal to the page), and the scale bar presented beside the pole figures refers to texture intensity of a random distribution **[50]**. Therefore, the stronger the texture, the greater the intensity. The centralized intensities on pole figure imply preferential orientation of a certain

set of grains **[51]**. The orientation of grains often follows the thermal gradient. High laser VED creates a localized heat accumulation that can make a homogeneous melting and dissolve most of the pre-existing heterogeneities in the former layer. As a result, there would be sufficient time for the grains to be oriented and grow against the heat transfer direction **[52]**. Therefore, several large elongated grains with a preferred orientation along the BD, are aligned and developed a predominant texture along {100} <101> (**Fig. 15(a-b)**). As discussed earlier, in the L-PBF fabricated SS316L samples, the predominant phase is austenite with FCC arrangement. According to solidification theory of FCC materials, <100> is the principal growth direction of this family of crystals. Since different crystallographic planes in FCC materials have distinct packing densities, solidification occurs along the direction with the least atomic aggregation due to faster heat dissipation **[33]**. Since the samples were produced using a stripe scanning strategy by 90º rotation, advance orientation of heat source and subsequently solidification direction frequently changes. On the other hand, the solidification of the last deposited layer starts from the bottom of the molten pool, because the transverse section of the already grown columnar grains would be an eligible site for heterogeneous nucleation. Hence, new grains tend to germinate on top of the previously formed grains and continue to grow epitaxially. Oftentimes, the angular deviation between the thermal gradient direction and the epitaxial growth is not substantial for disrupting the vertical growth of the columnar grains. Comparison of PF and IPF of the as-built sample (**Fig. 15(a-b)**), with annealed samples for 45 s (**Fig. 15(c-d)**) and 90 s (**Fig. 15(e-f)**) revealed that by annealing over 30 s, regardless of annealing time, spread texture is majorly attenuated. This effect can be verified through the comparison between the PF patterns before and after the annealing. In fact, after annealing for 45 s, maximum texture intensity is reduced from 28.3 to 10.6, while annealing up to 90 s led to a reduction in the texture intensity to 8.54. On the other hand, the maximum texture intensity of the IPF patterns is reduced from 8.66 in the as-built sample to 3.54 and 3.17 after annealing for 45 s and 90 s, respectively. Likewise, during annealing up to 90 s, the reduction in texture along the BD ({100}) is accompanied by a change in overall lattice orientation to other directions.

All the evidence implies a remarkable texture attenuation and gradual annihilation of the cellular structure. To find the origin of such behavior, the components of the cellular structures must be investigated as dissociated. According to the literature **[53]**, the cellular structure is composed of tubular columns with polygonal cross-section, with the walls of the

tubes made by intertwined dislocations, i.e. SGBs. Most of these intergranular tubes grow parallel to the grain boundaries and sometimes passes through multiple melt pools. Hence, they have a large aspect ratio which means the fraction of accumulated SGBs along the BD is much higher than its value in the perpendicular direction. As a result, gradual annihilation of the cellular structure during annealing leads to the removal of most of the aligned dislocation walls along BD. It must also be considered that the tubes orientation was influenced by the laser source and had different deviation angles with the BD, even if their general orientation was along BD. Sun et al. **[54]** indicated that the orientation of the grains with respect to growth direction could also contribute to developing the texture in the as-built SS316L samples. According to their observation, a lower deviation angle of the orientation of the grain with respect to BD could intensify the texture along {100} direction. Compared to zigzag epitaxial growth linked to the change in the growth angle in consecutive melt pools, straight growth of the grains can create more strong texture along the BD. Here, both EBSD patterns in **Fig. 14(a-c)** and OM micrographs in **Fig. 16** show that during annealing, in some melt pool borders, straight GBs evolved into a zigzag shape. This can be attributed to the faster lateral growth of the grains due to horizontal residual stress along the laser path. As a result, the variation of grains morphology from straight to zigzag could also contribute to texture attenuation during the annealing. However, even after annealing for 90 s, the grains kept their elongated shape aligned with the BD, suggesting that the zigzag boundaries were not playing a decisive role on texture debilitation, since after the annihilation of cellular structure over 45 s, the {100} direction was not the strongest anymore.

Indeed, dimensional and morphological changes of the grains during the rapid annealing were precisely evaluated, and the results are presented in **Fig. 16**. For a precise assessment of the grain growth mechanism during the high-temperature annealing, an extra sample was subjected to a heat treatment up to 300 s. The horizontal and vertical lengths of the highlighted grains were measured, and the grain size distribution along with the average length and width of the grains after different annealing times was presented. From the morphological insight, the as-built sample (**Fig. 16(a)**) had thin elongated grains with straight GBs and annealing for 30 s clearly increased the width of grains (**Fig. 16(b)**). In the following, by annealing for 90 s, 120 s, and 300 s (**Fig. 16(c-e)**) the grain growth sped up while the fraction of serrated boundaries increased, which can be ascribed to the lateral growth of the grains at the primary stages of the annealing.
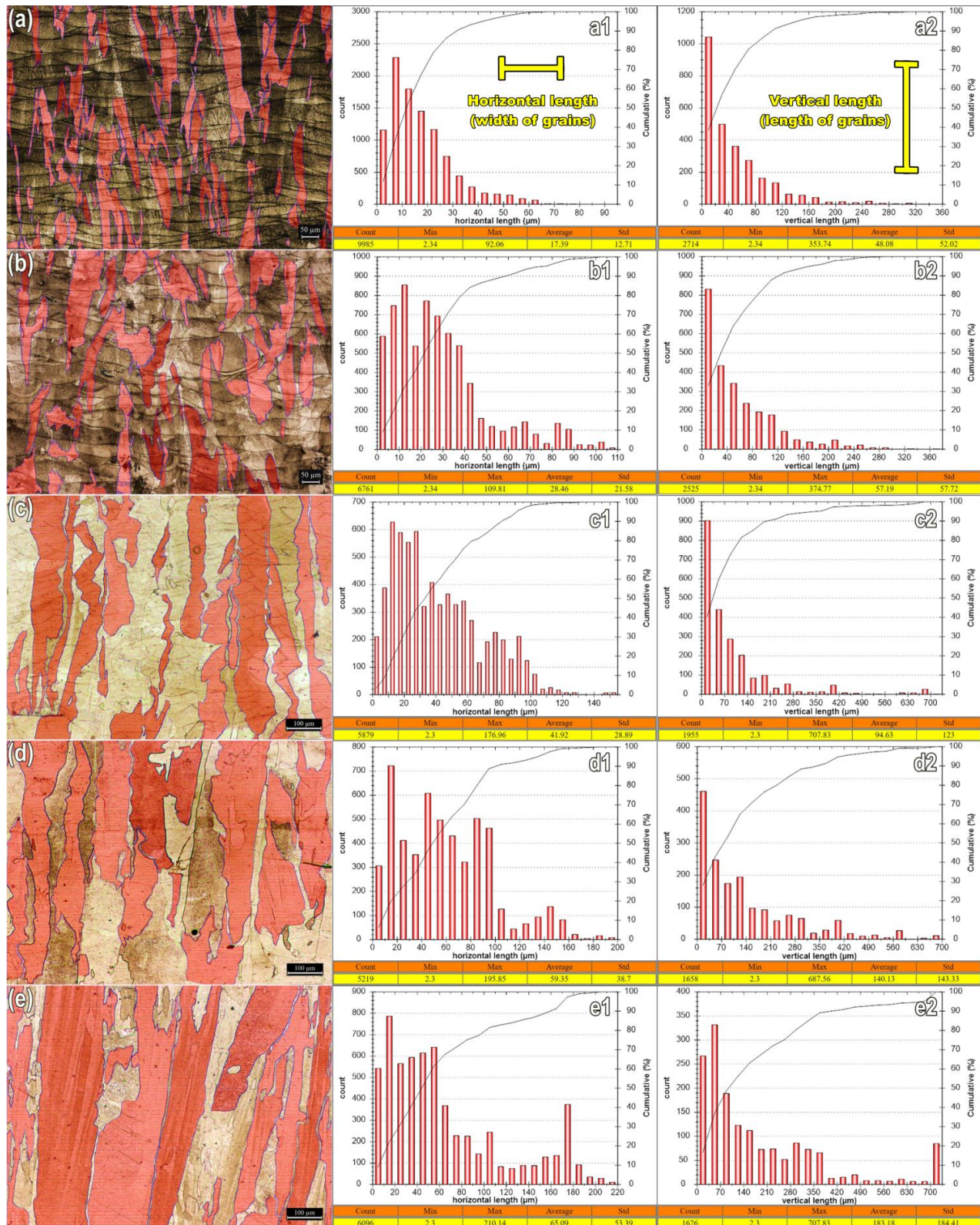
Fig. 16. Variation of the grains morphologies and horizontal and vertical length distribution of the grains in (a) as built sample and after annealing for (b) 30 s, (c) 90 s, (d) 120 s and (e) 300 s.

Variation of average width, length, and aspect ratio of the grains after rapid annealing for different times is presented in **Fig. 17**.
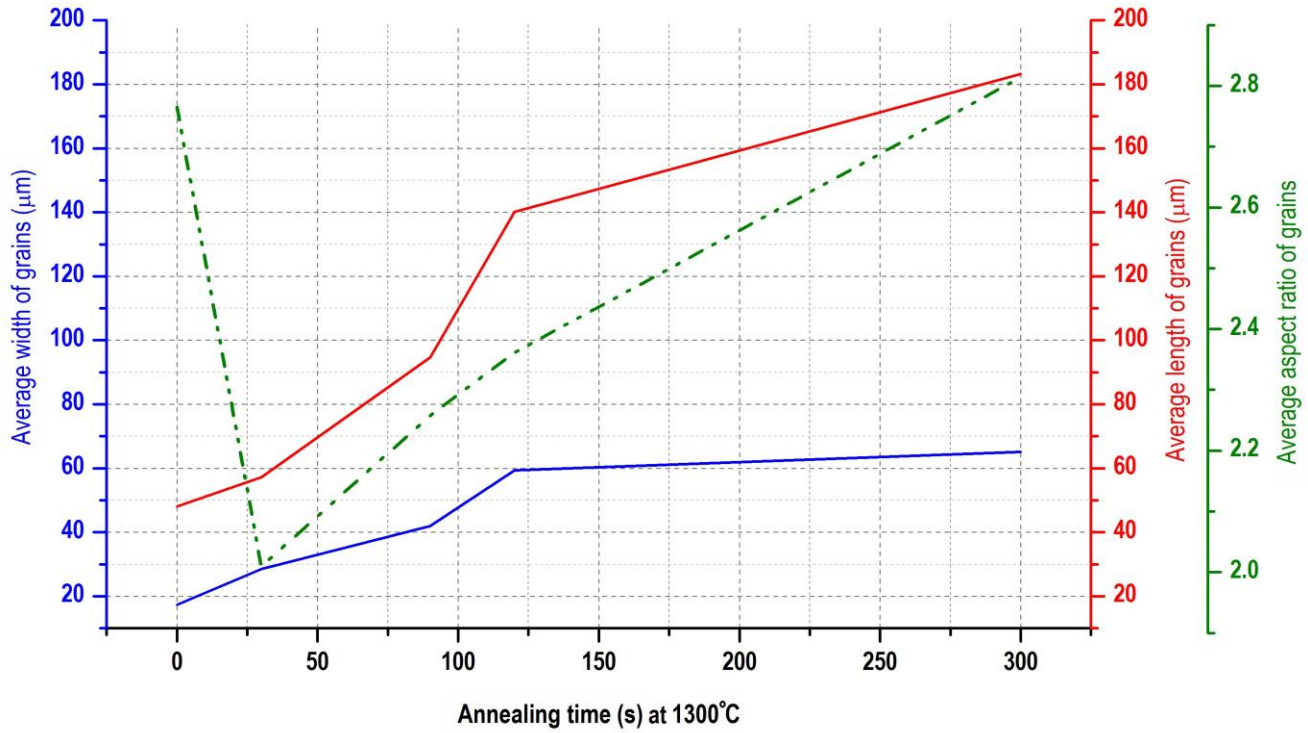

Fig. 17. Variation of the average length, width, and aspect ratio of the grains after annealing at 1300 ℃ up to 300 s.

As illustrated, annealing up to 300 s was constantly accompanied by horizontal (blue line) and vertical (red line) growth of the grains. At the beginning of the heat treatment, the rate of lateral growth along the laser trajectory surpassed the vertical counterpart. However, keep on annealing for longer times eventuated in greater grain growth along the BD along with annihilation of the SGBs (cell walls) and increment of the average aspect ratio of the grains. The curves show that the annealing for more than 30 s and the consequent annihilation of the cellular structure facilitate the stress relieving along the BD through the activation of the strain-induced grain boundary migration (SIGBM) mechanism. According to the literature [55], during the thermal recrystallization of samples having high residual stress, like in the case of severely strained materials, the grains prefer to grow toward the locations with maximum residual stress and stored energy. As a result, in materials with intensive texture and remarkable stored energy, often during annealing the grain growth along the length of elongated grains surpasses their transversal growth owing to SIGBM phenomenon.

2.4. Mechanical properties

Fig. 18 shows the effect of annealing time on the mechanical response of the L-PBF SS316L specimens for compression and tensile tests. Uniaxial compression loading was imposed along the building direction of the as-built specimens. As evident from the stress-strain curves in **Fig. 18(a-b)** and from the values presented in **Fig. 18(c)**, annealing for 10 s caused no measurable reduction of Yield Tensile Strength (YTS), Ultimate Tensile Strength (UTS), or Yield Compressive Strength (YCS). However, annealing for longer times resulted in an improvement in the elongation and a reduction in the mechanical strength with respect to the as-built specimens. Obviously, annealing up to 30 s has not significantly attenuated the tensile and compression strength of the samples. However, striking collapse in mechanical strength after annealing for 60 s is evident. By annealing of specimens for 30 s, YCS, YTS and UTS, declined from 305 MPa to 285 MPa (6%), from 530 to 455 MPa (14%) and from 681 to 637 MPa (6%), respectively. Instead, annealing for 60 s reduced the YCS, YTS and UTS values to 222 MPa (27%), 405 MPa (24%), and 579 MPa (15%), respectively. A similar downtrend for hardness **[56]** and tensile strength when increasing the annealing time **[17]** or temperature **[18]** was also reported by previous researchers. It is evident that the attenuation of mechanical strength by extending the annealing time concurs with the disintegration trend of the cellular network. Therefore, it is worthwhile to conclude that the interconnected cellular network acts like a scaffold pinned by nano-inclusions and ferrite stabilizer large atoms within the L-PBF printed SS316L sample. As long as this scaffolding network remains stable, the outstanding mechanical strength achieved as an advantage of L-PBF can almost be maintained. Instead, there is no doubt that rapid annealing for more than 30 s would eliminate the subgrains and reduce the strength, however increasing the ductility of the material. Nevertheless, the acquired properties after long-term annealing are not so impressive to suggest the use of longer heat treatments for L-PBF manufactured materials.
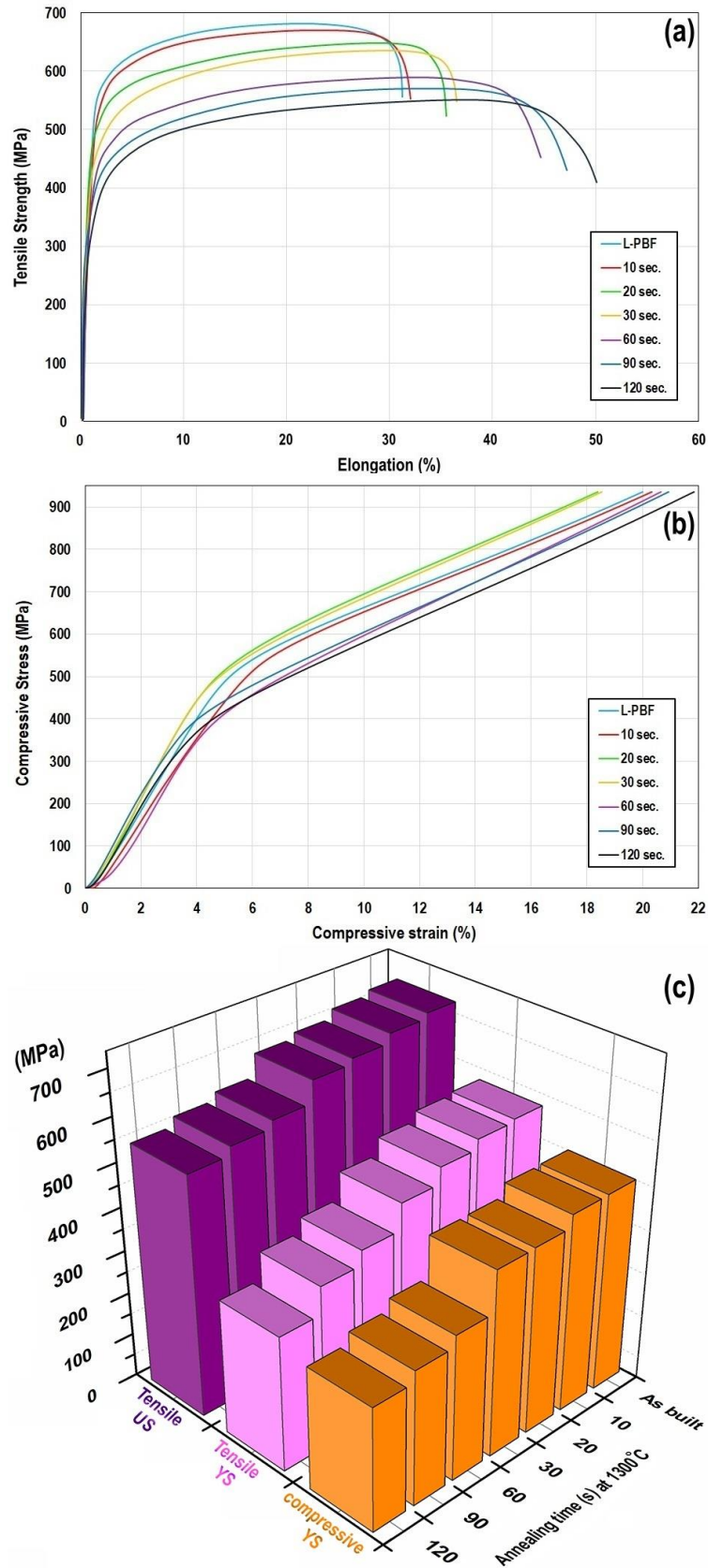
Fig. 18. (a) Tensile, (b) compressive stress-strain curves and (c) variation of the YCS, YTS and UTS by heat treatment at 1300 ºC for different periods.

Fig. 19 shows the fracture surface of the samples after the tensile test. As can be seen, the as-built sample (**Fig. 19(a)**) had the finest dimples and an increase in annealing time led to a partial growth of dimples in the fracture surfaces. Evidently, annealing up to 30 s could not majorly affect the size and morphology of dimples (**Fig. 19(b-d)**) while longer heat exposure increased the dimension of dimples (**Fig. 19(e-h)**). This behavior confirms that cellular structure can directly affect the strength of the material and its gradual elimination after 45 s reduces the number of dimple walls, which hints at a softer fracture.
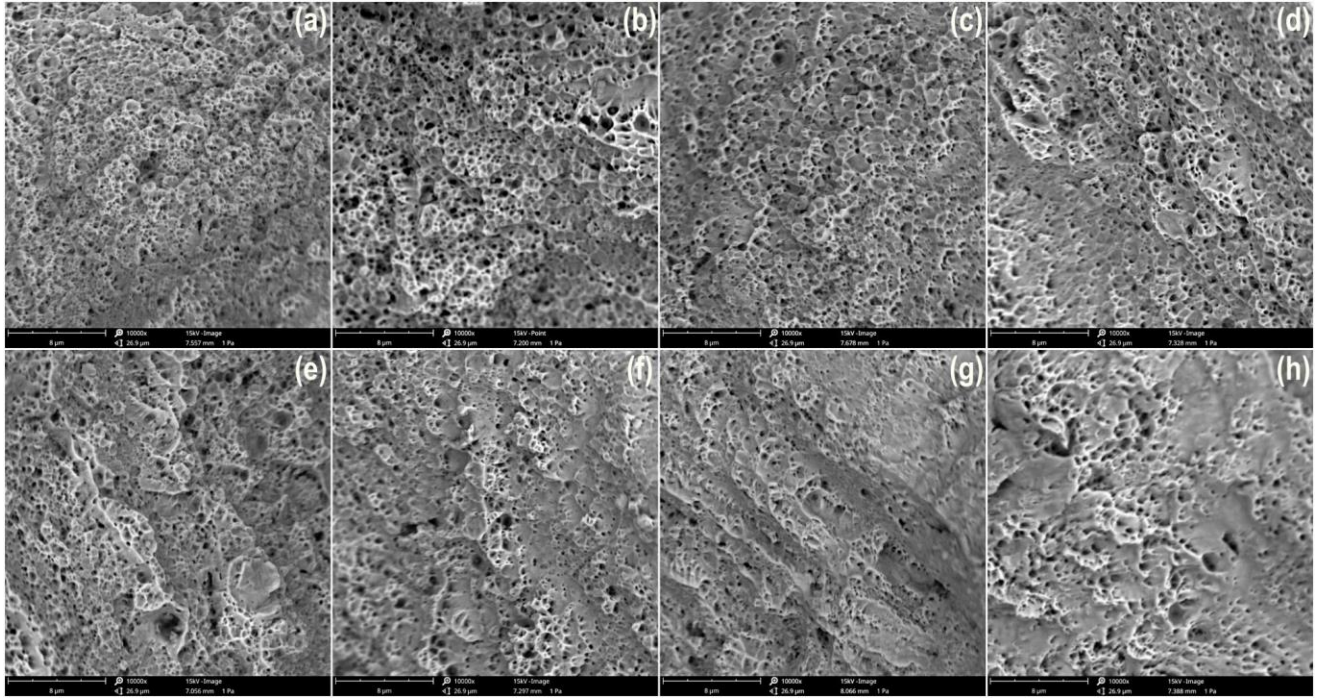

Fig. 19. Fracture surface of the (a) as-built sample, after annealing at 1300 °C for (b) 10 s, (c) 20 s, (d) 30 s, (e) 45 s, (f) 60 s, (g) 90 s, and (h) 120 s.

In-depth Characterization of the fracture surface (**Fig. 20**) shed light on the destructive role of some defects in the failure of the material. **Fig. 20(a)** shows that a long area has ruptured with a slip facture mode, which is a soft failure mechanism. Since the heat-affected zone (HAZ) of a laser track is the weakest point in the LPBF fabricated samples, probably this area was the HAZ of a laser track that has insufficient interfacial bonding and acted as crack origin under tensile loading. **Fig. 20(b)** shows that some inclusions were the origin of coarse dimples and contribute as one of the failure originations points. Similarly, some non-metallic inclusions with similar size and morphology were observed in OM micrographs during microstructural investigations (**Fig. 20(c)**). SEM analysis of the primary powder revealed that similar

inclusions were present on the surface of the particles from the beginning. The elemental distribution maps of **Fig. 20(d)** revealed that these inclusions were enriched in O and Si and probably have SiO$_2$ composition. It is proved that these large oxide inclusions inside the precursor powder formed during inert gas atomization were distinguished as the main origin of the formation of micro/nano inclusion in LPBF fabricated SS316L components. But owing to have a melting point (about 1710 °C) below the temperature of the laser beam, most of them were dissolved in molten pools under laser irradiation and formed again by re-oxidation/re-precipitation **[57, 58]**. Eventually, they remained in the steel matrix in the form of precipitates with negligible coherency and during the tensile test they could easily detach and create a void much larger than the typical dimple.
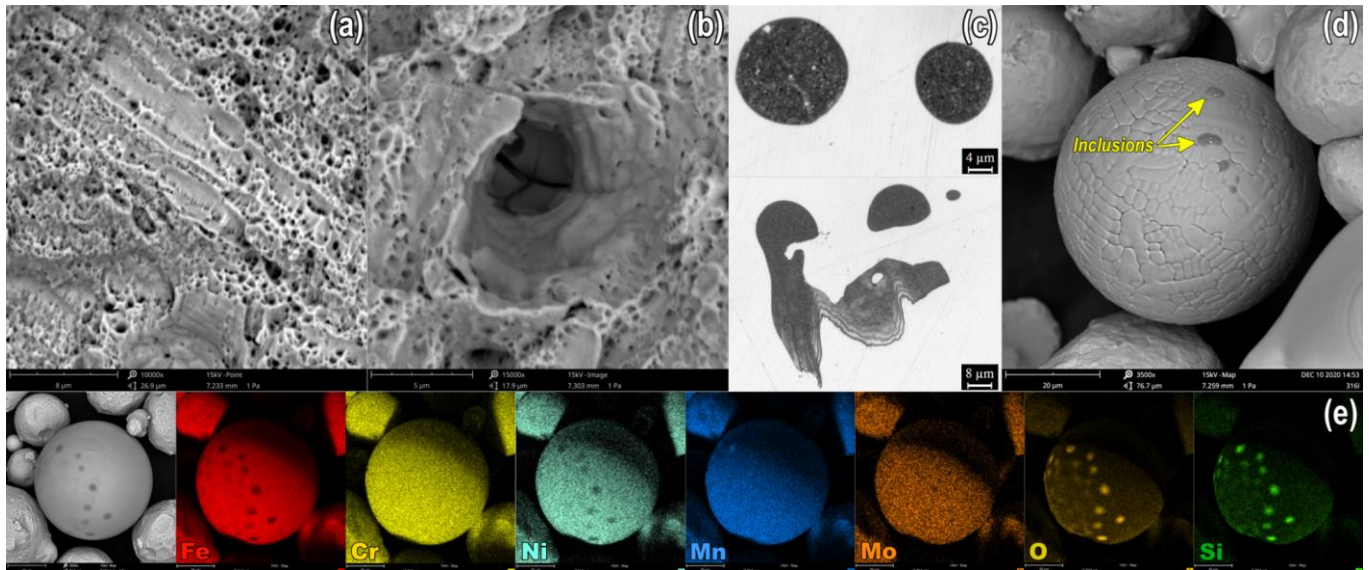
Fig. 20. (a) Trace of laser tracks on the fracture surface, and (b) the presence of SiO$_2$ inclusions in a dimple, (c) OM micrograph of as-built sample, (d) Surface of the initial powder, and (e) element distribution map of the primary powder.

3. Summary and conclusions

In the current study, samples of 316L austenitic steel were produced using the L-PBF technique. To identify a fast process to counteract strong texture formed due to the rapid solidification of fused layers, samples were treated via a short-term annealing (10-120 s) at 1300 °C. The effect of annealing time on the microstructure and mechanical strength of the

samples was evaluated. The main achievements of this research can be summarized as follows:

- ❖ An increment of the annealing time gradually causes the borders of melt pools to vanish and merged them together. SEM characterization revealed that the disappearance of the borders began after annealing for 45 s, and over 90 s most the laser footprints were removed, and grain growth accelerated.

- ❖ The monitoring of the disintegration of the cellular structure during rapid annealing indicated that the cell walls were stable up to 30 s and then were gradually annihilated. Thermal stability of the SGBs can be attributed to the presence of Mo, Cr, silicate inclusions, and a small amount of δ-ferrite, whose presence were validated by EDS and EBSD evidence.

- ❖ The severe thermal gradient from the surface to the depth of melt pools, and the change in the heat source direction during the buildup of samples, resulted in intensive epitaxial grain growth along the BD. EBSD outputs showed that a strong texture developed along the BD, that was largely thwarted by rapid annealing for more than 30 s. Since after annealing over 45 s the grains were still elongated, the texture reduction is instead attributed to the annihilation of the cellular structure as well as to the disordered transformation of straight GBs to zigzag shape.

- ❖ According to the analysis of the size and shape of the grains, by annealing over 30 s the grains started to grow faster along their length (BD), and their aspect ratio constantly increased. Due to remarkable residual stress along the BD, it can be attributed to the activation of SIGBM mechanism.

- ❖ Analysis of tensile and compressive properties of samples revealed that annealing up to 30 s would not significantly reduce the YCS (6%), YTS (14%) and UTS (6%). Whereas, annealing for 60 s lowered them about 27%, 24% and 15%, respectively. Comparing the mechanical outputs with the structural evolutions disclosed the undeniable scaffold-like role of SGBs on the mechanical strength of L-PBF fabricated SS316L samples.

References

[1] A.B. Kale, B.-K. Kim, D.-I. Kim, E. Castle, M. Reece, S.-H. Choi, An investigation of the corrosion behavior of 316L stainless steel fabricated by SLM and SPS techniques, Materials Characterization 163 (2020) 110204.

[2] C.F. Tey, X. Tan, S.L. Sing, W.Y. Yeong, Additive manufacturing of multiple materials by selective laser melting: Ti-alloy to stainless steel via a Cu-alloy interlayer, Additive Manufacturing 31 (2020) 100970.

[3] A. Saboori, A. Aversa, G. Marchese, S. Biamino, M. Lombardi, P. Fino, Microstructure and Mechanical Properties of AISI 316L Produced by Directed Energy Deposition-Based Additive Manufacturing: A Review, Applied Sciences 10(9) (2020) 3310.

[4] H. Pouraliakbar, G. Khalaj, M. Jandaghi, M. Khalaj, Study on the correlation of toughness with chemical composition and tensile test results in microalloyed API pipeline steels, Journal of Mining and Metallurgy B: Metallurgy 51(2) (2015) 173-178.

[5] A. Röttger, K. Geenen, M. Windmann, F. Binner, W. Theisen, Comparison of microstructure and mechanical properties of 316 L austenitic steel processed by selective laser melting with hot-isostatic pressed and cast material, Materials Science and Engineering: A 678 (2016) 365-376.

[6] G. Khalaj, H. Pouraliakbar, M.R. Jandaghi, A. Gholami, Microalloyed steel welds by HF-ERW technique: novel PWHT cycles, microstructure evolution and mechanical properties enhancement, International Journal of Pressure Vessels and Piping 152 (2017) 15-26.

[7] H. Pouraliakbar, G. Khalaj, M.R. Jandaghi, A. Fadaei, M.K. Ghareh-Shiran, S.H. Shim, S.I. Hong, Three-layered SS321/AA1050/AA5083 explosive welds: Effect of PWHT on the interface evolution and its mechanical strength, International Journal of Pressure Vessels and Piping 188 (2020) 104216.

[8] Y.M. Wang, T. Voisin, J.T. McKeown, J. Ye, N.P. Calta, Z. Li, Z. Zeng, Y. Zhang, W. Chen, T.T. Roehling, Additively manufactured hierarchical stainless steels with high strength and ductility, Nature materials 17(1) (2018) 63-71.

[9] A. Aversa, A. Saboori, E. Librera, M. de Chirico, S. Biamino, M. Lombardi, P. Fino, The Role of Directed Energy Deposition Atmosphere Mode on the Microstructure and Mechanical Properties of 316L Samples, Additive Manufacturing (2020) 101274.

[10] D. Kong, X. Ni, C. Dong, X. Lei, L. Zhang, C. Man, J. Yao, X. Cheng, X. Li, Bio-functional and anti-corrosive 3D printing 316L stainless steel fabricated by selective laser melting, Materials & Design 152 (2018) 88-101.

[11] M.H. Mosallanejad, B. Niroumand, A. Aversa, A. Saboori, In-situ alloying in laser-based additive manufacturing processes: A critical review, Journal of Alloys and Compounds (2021) 159567.

[12] H. Li, M. Ramezani, M. Li, C. Ma, J. Wang, Tribological performance of selective laser melted 316L stainless steel, Tribology International 128 (2018) 121-129.

[13] A. Charmi, R. Falkenberg, L. Ávila, G. Mohr, K. Sommer, A. Ulbricht, M. Sprengel, R.S. Neumann, B. Skrotzki, A. Evans, Mechanical anisotropy of additively manufactured stainless steel 316L: An experimental and numerical study, Materials Science and Engineering: A 799 (2021) 140154.

[14] E. Liverani, S. Toschi, L. Ceschini, A. Fortunato, Effect of selective laser melting (SLM) process parameters on microstructure and mechanical properties of 316L austenitic stainless steel, Journal of Materials Processing Technology 249 (2017) 255-263.

[15] Q. Zeng, K. Gan, Y. Wang, Effect of Heat Treatment on Microstructures and Mechanical Behaviors of 316L Stainless Steels Synthesized by Selective Laser Melting, Journal of Materials Engineering and Performance 30(1) (2021) 409-422.

[16] J. Kluczyński, L. Śnieżek, K. Grzelak, A. Oziębło, K. Perkowski, J. Torzewski, I. Szachogłuchowicz, K. Gocman, M. Wachowski, B. Kania, Comparison of different heat treatment processes of selective laser melted 316L steel based on analysis of mechanical properties, Materials 13(17) (2020) 3805.

[17] D. Kong, C. Dong, X. Ni, L. Zhang, J. Yao, C. Man, X. Cheng, K. Xiao, X. Li, Mechanical properties and corrosion behavior of selective laser melted 316L stainless steel after different heat treatment processes, Journal of Materials Science & Technology 35(7) (2019) 1499-1507.

[18] O. Salman, C. Gammer, A. Chaubey, J. Eckert, S. Scudino, Effect of heat treatment on microstructure and mechanical properties of 316L steel synthesized by selective laser melting, Materials Science and Engineering: A 748 (2019) 205-212.

[19] T. Ronneberg, C.M. Davies, P.A. Hooper, Revealing relationships between porosity, microstructure and mechanical properties of laser powder bed fusion 316L stainless steel through heat treatment, Materials & Design 189 (2020) 108481.

[20] J. Reijonen, R. Björkstrand, T. Riipinen, Z. Que, S. Metsä-Kortelainen, M. Salmi, Cross-testing laser powder bed fusion production machines and powders: Variability in mechanical properties of heat-treated 316L stainless steel, Materials & Design 204 (2021) 109684.

[21] Q. Chao, S. Thomas, N. Birbilis, P. Cizek, P.D. Hodgson, D. Fabijanic, The effect of post-processing heat treatment on the microstructure, residual stress and mechanical properties of selective laser melted 316L stainless steel, Materials Science and Engineering: A 821 (2021) 141611.

[22] D. Riabov, A. Leicht, J. Ahlström, E. Hryha, Investigation of the strengthening mechanism in 316L stainless steel produced with laser powder bed fusion, Materials Science and Engineering: A 822 (2021) 141699.

[23] T. Voisin, J.-B. Forien, A. Perron, S. Aubry, N. Bertin, A. Samanta, A. Baker, Y.M. Wang, New insights on cellular structures strengthening mechanisms and thermal stability of an austenitic stainless steel fabricated by laser powder-bed-fusion, Acta Materialia 203 (2021) 116476.

[24] S. Dryepondt, P. Nandwana, P. Fernandez-Zelaia, F. List III, Microstructure and high temperature tensile properties of 316L fabricated by laser powder-bed fusion, Additive Manufacturing 37 (2021) 101723.

[25] H. Yin, M. Song, P. Deng, L. Li, B.C. Prorok, X. Lou, Thermal stability and microstructural evolution of additively manufactured 316L stainless steel by laser powder bed fusion at 500–800℃, Additive Manufacturing 41 (2021) 101981.

[26] C. Zhou, S. Hu, Q. Shi, H. Tao, Y. Song, J. Zheng, P. Xu, L. Zhang, Improvement of corrosion resistance of SS316L manufactured by selective laser melting through subcritical annealing, Corrosion Science 164 (2020) 108353.

[27] S. Waqar, J. Liu, Q. Sun, K. Guo, J. Sun, Effect of post-heat treatment cooling on microstructure and mechanical properties of selective laser melting manufactured austenitic 316L stainless steel, Rapid Prototyping Journal (2020).

[28] G. Miranda, S. Faria, F. Bartolomeu, E. Pinto, S. Madeira, A. Mateus, P. Carreira, N. Alves, F. Silva, O. Carvalho, Predictive models for physical and mechanical properties of 316L stainless steel produced by selective laser melting, Materials Science and Engineering: A 657 (2016) 43-56.

[29] L. Löber, C. Flache, R. Petters, U. Kühn, J. Eckert, Comparison of different post processing technologies for SLM generated 316l steel parts, Rapid Prototyping Journal (2013).

[30] Y. Zhang, J. Zhang, Modeling of solidification microstructure evolution in laser powder bed fusion fabricated 316L stainless steel using combined computational fluid dynamics and cellular automata, Additive Manufacturing 28 (2019) 750-765.

[31] K.V. Yang, P. Rometsch, T. Jarvis, J. Rao, S. Cao, C. Davies, X. Wu, Porosity formation mechanisms and fatigue response in Al-Si-Mg alloys made by selective laser melting, Materials Science and Engineering: A 712 (2018) 166-174.

[32] T. Heeling, K. Wegener, The effect of multi-beam strategies on selective laser melting of stainless steel 316L, Additive Manufacturing 22 (2018) 334-342.

[33] O. Andreau, I. Koutiri, P. Peyre, J.-D. Penot, N. Saintier, E. Pessard, T. De Terris, C. Dupuy, T. Baudin, Texture control of 316L parts by modulation of the melt pool morphology in selective laser melting, Journal of Materials Processing Technology 264 (2019) 21-31.

[34] R. Shi, S.A. Khairallah, T.T. Roehling, T.W. Heo, J.T. McKeown, M.J. Matthews, Microstructural control in metal laser powder bed fusion additive manufacturing using laser beam shaping strategy, Acta Materialia 184 (2020) 284-305.

[35] U. Scipioni Bertoli, B.E. MacDonald, J.M. Schoenung, Stability of cellular microstructure in laser powder bed fusion of 316L stainless steel, Materials Science and Engineering: A 739 (2019) 109-117.

[36] K. Saeidi, X. Gao, Y. Zhong, Z.J. Shen, Hardened austenite steel with columnar sub-grain structure formed by laser melting, Materials Science and Engineering: A 625 (2015) 221-229.

[37] A. Saboori, G. Piscopo, M. Lai, A. Salmi, S. Biamino, An investigation on the effect of deposition pattern on the microstructure, mechanical properties and residual stress of 316L produced by Directed Energy Deposition, Materials Science and Engineering: A 780 (2020) 139179.

[38] H.S. Kim, Y. Kobayashi, S. Tsukamoto, K. Nagai, Effect of cooling rate on microstructure evolution of rapidly cooled high-impurity steels, Materials Science and Engineering: A 403(1-2) (2005) 311-317.

[39] H. Yin, S. Felicelli, Dendrite growth simulation during solidification in the LENS process, Acta Materialia 58(4) (2010) 1455-1465.

[40] P. HOCHNADEL, M.J. Cola, Pulsed Laser Beam Welding of 304 to 304L Stainless Steel: Effects of Welding Parameters on Cracking and Phase Transformations, Los Alamos National Lab., NM (US), 2001.

[41] M. Ma, Z. Wang, X. Zeng, A comparison on metallurgical behaviors of 316L stainless steel by selective laser melting and laser cladding deposition, Materials Science and Engineering: A 685 (2017) 265-273.

[42] C. Man, C. Dong, T. Liu, D. Kong, D. Wang, X. Li, The enhancement of microstructure on the passive and pitting behaviors of selective laser melting 316L SS in simulated body fluid, Applied Surface Science 467-468 (2019) 193-205.

[43] Y. Zhong, L. Liu, S. Wikman, D. Cui, Z. Shen, Intragranular cellular segregation network structure strengthening 316L stainless steel prepared by selective laser melting, Journal of Nuclear Materials 470 (2016) 170-178.

[44] K. Bertsch, G.M. de Bellefon, B. Kuehl, D. Thoma, Origin of dislocation structures in an additively manufactured austenitic stainless steel 316L, Acta Materialia 199 (2020) 19-33.

[45] B. Kocabekir, R. Kaçar, S. Gündüz, F. Hayat, An effect of heat input, weld atmosphere and weld cooling conditions on the resistance spot weldability of 316L austenitic stainless steel, Journal of Materials Processing Technology 195(1) (2008) 327-335.

[46] P. Guo, B. Zou, C. Huang, H. Gao, Study on microstructure, mechanical properties and machinability of efficiently additive manufactured AISI 316L stainless steel by high-power direct laser deposition, Journal of Materials Processing Technology 240 (2017) 12-22.

[47] A. Saboori, A. Aversa, F. Bosio, E. Bassini, E. Librera, M. De Chirico, S. Biamino, D. Ugues, P. Fino, M. Lombardi, An investigation on the effect of powder recycling on the microstructure and mechanical properties of AISI 316L produced by Directed Energy Deposition, Materials Science and Engineering: A 766 (2019) 138360.

[48] X.-q. Ni, D. Kong, Y. Wen, L. Zhang, W.-h. Wu, B.-b. He, L. Lu, D.-x. Zhu, Anisotropy in mechanical properties and corrosion resistance of 316L stainless steel fabricated by selective laser melting, International Journal of Minerals, Metallurgy, and Materials 26 (2019) 319-328.

[49] B. Barkia, P. Aubry, P. Haghi-Ashtiani, T. Auger, L. Gosmain, F. Schuster, H. Maskrot, On the origin of the high tensile strength and ductility of additively manufactured 316L stainless steel: Multiscale investigation, Journal of Materials Science & Technology 41 (2020) 209-218.

[50] H. Choo, K.-L. Sham, J. Bohling, A. Ngo, X. Xiao, Y. Ren, P. Depond, M. Matthews, E. Garlea, Effect of laser power on defect, texture, and microstructure of a laser powder bed fusion processed 316L stainless steel, Materials & Design 164 (2018).

[51] E. Garlea, H. Choo, C.C. Sluss, M.R. Koehler, R.L. Bridges, X. Xiao, Y. Ren, B.H. Jared, Variation of elastic mechanical properties with texture, porosity, and defect characteristics in laser powder bed fusion 316L stainless steel, Materials Science and Engineering: A 763 (2019) 138032.

[52] M. Ghayoor, K. Lee, Y. He, C.-h. Chang, B.K. Paul, S. Pasebani, Selective laser melting of 304L stainless steel: Role of volumetric energy density on the microstructure, texture and mechanical properties, Additive Manufacturing 32 (2020) 101011.

[53] M. Godec, S. Zaefferer, B. Podgornik, M. Šinko, E. Tchernychova, Quantitative multiscale correlative microstructure analysis of additive manufacturing of stainless steel 316L processed by selective laser melting, Materials Characterization 160 (2020) 110074.

[54] Z. Sun, X. Tan, S.B. Tor, C.K. Chua, Simultaneously enhanced strength and ductility for 3D-printed stainless steel 316L by selective laser melting, NPG Asia Materials 10(4) (2018) 127-136.

[55] H. Pouraliakbar, M.R. Jandaghi, G. Khalaj, Constrained groove pressing and subsequent annealing of Al-Mn-Si alloy: Microstructure evolutions, crystallographic transformations, mechanical properties, electrical conductivity and corrosion resistance, Materials & Design (2017).

[56] P. Krakhmalev, I. Yadroitsava, G. Fredriksson, I. Yadroitsev, Microstructural and thermal stability of selective laser melted 316L stainless steel single tracks, South African Journal of Industrial Engineering 28 (2017).

[57] A. Saboori, M. Toushekhah, A. Aversa, M. Lai, M. Lombardi, S. Biamino, P. Fino, Critical features in the microstructural analysis of AISI 316L produced by metal additive manufacturing, Metallography, Microstructure, and Analysis 9(1) (2020) 92-96.

[58] P. Deng, M. Karadge, R.B. Rebak, V.K. Gupta, B.C. Prorok, X. Lou, The origin and formation of oxygen inclusions in austenitic stainless steels manufactured by laser powder bed fusion, Additive Manufacturing 35 (2020) 101334.